Channel Estimation for Reconfigurable Intelligent Surface-aided 6G NOMA Systems: A Quantum Machine Learning Approach

Nhien Q. T. Thoong, *Graduate Student Member, IEEE*, Adnan A. Cheema, *Senior Member, IEEE*, Berk Canberk, *Senior Member, IEEE*, Dung Thanh Tran, *Graduate Student Member, IEEE*, Octavia A. Dobre, *Fellow, IEEE*, Trung Q. Duong, *Fellow, IEEE*

***Abstract*—The integration of reconfigurable intelligent surfaces (RISs) and non-orthogonal multiple access (NOMA) is considered a promising technique to enhance spectral efficiency and connectivity in future 6G networks. Accurate channel estimation remains a critical challenge in RIS-NOMA systems due to the increased complexity introduced by the combination of RIS and NOMA technologies. While quantum machine learning (QML) has demonstrated potential in wireless communications, its application in channel estimation remains underexplored. This paper investigates the effectiveness of a hybrid quantum-classical machine learning (ML) model for channel estimation in RIS-NOMA systems. We propose a hybrid architecture that integrates convolutional neural networks (CNNs) with quantum long short-term memory (QLSTM) networks, where CNNs perform spatial feature extraction while QLSTMs capture temporal dependencies in the time-varying channel. Extensive simulations are conducted to evaluate the performance of the model under various network configurations, considering different power allocation factors, the number of RIS elements, and signal-to-noise ratios (SNRs). The performance of the proposed model is benchmarked against both pure quantum and classical ML models, including a quantum neural network (QNN), a CNN, a long short-term memory (LSTM) model, a bidirectional LSTM (BiLSTM) model, and a CNN-LSTM model. The results demonstrate that the proposed CNN-QLSTM model outperforms all baseline methods in terms of root mean square error (RMSE), mean absolute error (MAE), and mean absolute percentage error (MAPE). These findings highlight the potential of quantum-enhanced ML for channel estimation in next-generation communication networks.**

***Index Terms*—Channel estimation, quantum machine learning (QML), CNN, QLSTM, NOMA, RIS, 6G networks.**

I. Introduction

The sixth-generation (6G) wireless communication networks are attracting global attention from both academia and industry, driven by the need to overcome the limitations of previous communication networks, such as fifth-generation (5G). 6G is expected to significantly enhance reliability, coverage, latency, speed, and sensing accuracy, surpassing the capabilities of its predecessors [1]. These advancements are built upon emerging technologies such as terahertz (THz) frequency bands [2], advanced multiple-input multiple-output (MIMO) systems [3], artificial intelligence (AI) [4], and quantum computing, which collectively contribute to the unprecedented performance of 6G. With these enhanced capabilities, 6G aims to facilitate a wide range of mission-critical applications that require ultra-reliable and low-latency communications, e.g., augmented reality (AR), extended reality (XR), virtual reality (VR), robotics and autonomous systems, connected health, and holographic or tactile communications. Furthermore, 6G is expected to support the Internet of Everything (IoE) by seamlessly integrating a diverse array of devices and systems, which will create intelligent and interconnected environments across various sectors, including smart cities and industrial automation. A key enabler of this vision is the integration of non-terrestrial networks (NTN) and terrestrial networks (TN), which ensures seamless connectivity and expands the capabilities of IoE across remote and urban areas. This integration not only ensures ubiquitous and seamless connectivity across both urban and remote areas but also enhances network robustness, scalability, and low-latency communications essential for IoE applications. The fusion of NTN and TN accelerates the realization of innovative IoE applications, enabling a fully connected ecosystem that spans from the molecular to the universal scale [5].

To fully harness the potential of 6G in supporting these diverse mission-critical applications, traditional orthogonal multiple access (OMA) approaches are insufficient since they struggle to accommodate the massive number of users and devices expected in 6G networks due to their inflexible

N. Q. T. Thoong and O. A. Dobre are with the Faculty of Engineering and Applied Science, Memorial University, St. John's, NL A1B 3X5, Canada (e-mail: qtnthoong, odobre@mun.ca).

A. A. Cheema is with the School of Engineering, Ulster University, BT15 1AP Belfast, U.K. (e-mail: a.cheema@ulster.ac.uk).

B. Canberk is with the School of Computing, Engineering and Built Environment, Edinburgh Napier University, Edinburgh EH10 5DT, U.K. (e-mail: b.canberk@napier.ac.uk).

D. T. Tran is with Duy Tan University, Da Nang 50000, Vietnam

T. Q. Duong is with the Faculty of Engineering and Applied Science, Memorial University, St. John's, NL A1C 5S7, Canada, and also with the School of Electronics, Electrical Engineering and Computer Science, Queen's University Belfast, BT7 1NN Belfast, U.K. (e-mail: tduong@mun.ca).

This paper has been accepted in part for presentation at the 2024 IEEE 100th Vehicular Technology Conference (VTC2024-Fall), October 2024, Washington, DC, USA, DOI: 10.1109/VTC2024-Fall63153.2024.10757552.

This work was supported in part by the Canada Excellence Research Chair (CERC) Program CERC-2022-00109, in part by the Natural Sciences and Engineering Research Council of Canada (NSERC) Discovery Grant Program RGPIN-2025-04941, and in part by the NSERC Collaborative Research and Training Experience (CREATE) Program (Grant number 596205-2025). The work of O. A. Dobre was supported in part by the Canada Research Chair Program CRC-2022-00187. The work of B. Canberk was partially supported by The Scientific and Technological Research Council of Turkey (TUBITAK) 1515 Frontier R&D Laboratories Support Program for BTS Advanced AI Hub: BTS Autonomous Networks and Data Innovation Lab. Project 5239903.

T. Q. Duong is the corresponding author.

resource allocation mechanisms [6]. To address the growing demands for ultra-reliable, low-latency communication, and enhanced connectivity, non-orthogonal multiple access (NOMA) emerges as a promising solution [7]. Unlike OMA, NOMA allows multiple users to simultaneously share the same radio resources (e.g., frequency bands) by separating them in either the power or code domain. This capability enables NOMA to meet the massive connectivity requirements of 6G networks while maintaining fairness among users, making it a key enabler for efficient and scalable resource allocation. Recent studies have shown that NOMA can provide substantial benefits over traditional OMA techniques, including improved spectral and energy efficiency, which are essential for achieving the high data rates and low latency goals of 6G [8]. As 6G development progresses, achieving effective integration of NOMA with emerging technologies such as reconfigurable intelligent surfaces (RISs), advanced MIMO, millimeter-wave (mmWave), and AI remains an open research question, which must be addressed to fully realize the ambitious goals of 6G networks.

In recent years, RISs have gained significant attention within the research community as a promising technique for enhancing network coverage, connectivity, and overall performance in 6G systems [9]. RIS technology facilitates various wireless functions, including communication, power transfer, sensing, and localization, and is therefore considered a key enabler for 6G, alongside other emerging technologies, such as orthogonal time frequency space (OTFS), THz frequency bands, and integrated sensing and communication (ISAC) [10]. By dynamically adjusting the phase and the amplitude of its reflective elements, a RIS can modify wireless propagation environments to enhance signal strength, reduce interference, and improve energy efficiency, leading to more efficient and reliable wireless networks [11]. The combination of NOMA and RIS has the potential to significantly improve network performance by leveraging the strengths of both technologies. Specifically, a RIS can effectively mitigate the limitations of NOMA by optimally increasing the channel gain differences among users. Through strategic placement and reflection coefficient adjustments, a RIS can enhance the performance of power-domain NOMA, allowing for significant improvements in its overall performance and achievable gains [12]. However, the successful deployment of RIS in 6G networks requires addressing challenges related to channel estimation, real-time control of RIS elements, and the development of efficient algorithms to manage the interplay between RIS and NOMA. Ongoing research efforts are focusing on addressing these challenges to fully exploit the synergistic potential of RIS and NOMA for future 6G networks.

A wireless channel is a physical medium through which wireless signals propagate between a transmitter and a receiver [13], [14]. Accurate estimation of channel state information (CSI) is crucial in a 6G communication system, especially in a RIS-NOMA system where scattering, multi-path propagation, power decay, and shadowing effects are highly unpredictable. CSI provides comprehensive information about channel characteristics, such as fading coefficients, delay spreads, and Doppler shifts, which are essential for optimizing signal transmission and reception. Precise CSI estimation enables the system to adaptively adjust parameters to mitigate the effects of channel fading and manage interference. This leads to enhanced signal quality and increased data transmission rates [15]. In NOMA systems, achieving accurate CSI is indispensable for executing successive interference cancellation (SIC) at each receiver [16]. SIC relies on the accurate decoding of superimposed signals from multiple users sharing the same radio resources. Without precise CSI, the effectiveness of SIC diminishes, resulting in increased error rates and degraded system performance. Moreover, a RIS typically comprises a large number of elements, each capable of independently adjusting the phase and amplitude of the incoming signals. This results in a complex and high-dimensional channel environment, where a multitude of channel parameters need to be estimated simultaneously. The large number of parameters significantly increases the complexity and computational load of CSI estimation, making it even more challenging in RIS-enhanced NOMA systems [17]. Advanced techniques are being explored to address these challenges, including machine learning (ML)-based approaches, compressive sensing, and distributed estimation algorithms [18], [19], [20].

Quantum technology is initiating a transformative change in the field of computing. Quantum computations are performed using circuits composed of parameterized quantum gates, which can be trained or optimized by classical optimization methods. As a result, the quantum machine learning (QML) framework has gained increasing attention across various disciplines [21]. In QML, classical data is embedded into quantum bits (qubits), leveraging quantum phenomena such as superposition and entanglement to potentially reduce the size of neural networks and accelerate the training process [22]. This novel paradigm offers significant computational advantages across various domains, enabled by quantum computers that can process multiple states simultaneously through quantum parallelism. In the context of 6G wireless communication, QML shows potential for solving complex, real-time computing tasks such as signal processing, resource allocation, network traffic optimization, and channel estimation [23]. The ability of QML to handle large-scale data and perform parallel computations could lead to more efficient and scalable solutions in these areas. However, despite its potential, the practical application of QML in channel estimation remains largely underexplored in the existing literature. Current studies have primarily focused on theoretical frameworks and preliminary experiments, with limited empirical evaluations in real-world 6G scenarios. Challenges such as quantum noise, qubit decoherence, and the limited number of qubits in current quantum hardware hinder the practical deployment of QML algorithms. Additionally, developing efficient quantum algorithms that can operate within these hardware constraints while achieving performance improvements is an ongoing area of research.

The convergence of these technologies presents both significant opportunities and challenges for future wireless communications. RIS technology offers unprecedented control over wireless propagation environments, whilst NOMA enables efficient spectrum utilisation through non-orthogonal resource sharing. Meanwhile, QML emerges as a promising paradigm

that can potentially address the computational complexities of next-generation wireless systems through quantum parallelism and enhanced processing capabilities. However, the integration of these technologies introduces new technical challenges, particularly in channel estimation, which remains a critical enabler for optimal system performance. The complex interplay between RIS reflection characteristics, NOMA power allocation strategies, and dynamic channel conditions creates a sophisticated estimation problem that requires innovative solutions.

II. Motivation and Contributions

This section presents the specific motivations driving our research and details the key contributions of this work. The increasing complexity of 6G wireless networks, with the integration of RIS and NOMA, introduces challenges in channel estimation, including high-dimensional channel matrices and dynamic time-varying environments. While these technologies offer substantial benefits individually, their combination creates unprecedented estimation complexity that existing approaches struggle to address effectively. Traditional and ML-based methods offer partial solutions, but they remain limited by scalability challenges and computational demands, especially as the number of users and RIS elements increases. Despite the promising potential of QML, QML-based channel estimation techniques for RIS-NOMA systems remain largely unexamined in existing literature. To address this critical research gap, this work takes an initial step in investigating the feasibility of QML for channel estimation in RIS-NOMA downlink systems. In this paper, we propose a convolutional quantum long short-term memory (CNN-QLSTM) architecture, a QML-based channel estimation method that integrates CNNs with quantum long short-term memory (QLSTM) networks to enhance estimation accuracy. One of the key strengths of the CNN architecture is its ability to perform automatic feature extraction [24], making it particularly useful for handling high-dimensional channel coefficient matrices in RIS-NOMA systems, where the presence of multiple users and numerous RIS elements significantly increases estimation complexity. Meanwhile, the LSTM architecture effectively captures long-term dependencies in sequential wireless channel data [25], [26]. The integration of quantum computing with LSTM through variational quantum circuits (VQCs) allows QLSTM to exploit quantum parallelism [27], which potentially improves the efficiency of processing complex channel dynamics in RIS-NOMA systems. The main contributions of this paper are summarized in Tab. I and listed as follows:

- We investigate a downlink RIS-NOMA communication system considering both large-scale and small-scale fading to reflect realistic propagation conditions. The system applies power-domain NOMA and uses a passive RIS to assist the transmission.
- A hybrid quantum-classical ML framework is proposed for channel estimation in RIS-NOMA downlink systems. The CNN-QLSTM model combines CNNs for spatial feature extraction with QLSTM networks to capture temporal variations in wireless channels. This hybrid approach enables effective handling of high-dimensional channel matrices and dynamic time-varying environments in RIS-NOMA networks.
- To ensure the robustness and efficiency of the proposed QML model, we evaluate multiple quantum circuit architectures with varying numbers of qubits and different quantum embedding techniques. Extensive simulations are conducted to determine the optimal configuration that balances estimation accuracy and computational efficiency in the RIS-NOMA channel estimation task.
- The performance of the proposed CNN-QLSTM model is evaluated under various network configurations. The study examines how estimation accuracy is influenced by signal strength, power allocation factors, and the number of RIS elements.
- The proposed CNN-QLSTM model is compared with both pure quantum and conventional DL-based estimators, including quantum neural network (QNN), CNN, LSTM, and BiLSTM models. The results demonstrate that CNN-QLSTM achieves the lowest estimation errors across different evaluation metrics. This result highlights the superiority of hybrid architectures over pure quantum methods and demonstrates the effectiveness of our approach in improving channel estimation accuracy in RIS-NOMA systems.

TABLE I: Overview of prior studies and this work.

Studies	RIS	NOMA	QML
[28]–[30]	✓	×	×
[31]–[33]	×	✓	×
[34], [35]	✓	✓	×
[36]	×	×	✓
[37]	✓	×	✓
This work	✓	✓	✓

The remainder of this paper is structured as follows. Section III reviews related works on channel estimation techniques, RIS-NOMA systems, and quantum technologies for 6G. Section IV presents the RIS-NOMA system model and formulates the channel estimation problem. Section V proposes the CNN-QLSTM model as a QML-based solution for channel estimation. Section VI presents the evaluation results under various RIS-NOMA system configurations. Finally, Section VII concludes the paper with key findings and potential directions for future research.

III. Related Works

To contextualise our contribution, this section reviews the literature across three key areas. We begin by surveying the evolution of channel estimation techniques. Next, we discuss broader system-level studies on RIS-aided NOMA systems. Finally, we provide an overview of emerging quantum technologies for 6G, which establishes the foundation for our proposed QML approach.

A. Channel Estimation Techniques

ML has gained increasing attention in channel estimation as a data-driven approach that complements traditional

model-based methods. By leveraging data-driven models, ML techniques offer new possibilities for improving estimation accuracy and adaptability in diverse channel conditions. This section reviews the progression from foundational classical methods to advanced ML and emerging QML approaches. Conventional channel estimation relies on classical signal processing and statistical methods. For NOMA systems, adaptive algorithms have been explored. [31] introduced a variable forgetting factor recursive least square (VFFRLS) algorithm for channel estimation in NOMA systems. By adaptively adjusting the forgetting factor, the algorithm improved estimation accuracy and convergence speed compared to the conventional recursive least square (RLS) algorithm. In [32], an arctangent least mean square (ATLMS) algorithm was developed for channel estimation in NOMA-orthogonal frequency-division multiplexing (OFDM) systems. The results indicated improved performance over the traditional least mean square (LMS) technique in terms of spectral efficiency and convergence stability. For RIS-aided systems, an MMSE-based interpolation technique was proposed for RIS-aided channel estimation in [28]. The proposed method modelled multiplicative fading correlation functions and employed an ON/OFF-based MMSE estimation strategy to mitigate error floors associated with traditional approaches. Simulation results indicated that the method enhanced estimation accuracy and power efficiency, particularly for high-speed users near the cell edge. While foundational, these classical methods often rely on simplified channel models and can lack the robustness needed for the combined complexity of a joint RIS-NOMA system, which motivated the shift toward ML-based solutions. General ML-based channel estimation approaches have been extensively explored across various wireless communication systems, demonstrating consistent improvements over traditional methods but with varying computational complexity trade-offs. A study in [15] presented an ML-based approach for channel estimation in the uplink of 5G New Radio (NR) systems. The proposed method integrated an online training scheme that allowed continuous adaptation to dynamic channel conditions. Performance evaluation using normalised mean square error (NMSE) and bit error rate (BER) showed that the method outperformed LS and linear ML (LML)-based estimation, especially in higher-order modulation schemes. A residual network with an attention mechanism was presented in [38] to enhance LS-based channel estimation by suppressing noise while preserving channel information. This method demonstrated improved accuracy and robustness compared to conventional LS and linear MMSE (LMMSE) approaches, particularly in low-SNR conditions. However, these general approaches primarily focused on single-antenna or simple MIMO configurations, limiting their applicability to more complex wireless architectures. Advanced neural network architectures have shown particular promise for complex channel environments, though they require substantial computational resources and training data. In [39], a stacked denoising autoencoder (SDAE)-based DNN was developed to estimate channel parameters in chaotic wireless systems without requiring pilot signals. This method leveraged the autocorrelation function (ACF) of received signals to enhance estimation accuracy while reducing bandwidth consumption. Simulation results demonstrated improved mean square error (MSE) and BER performance compared to LS and blind ACF-based estimation methods. In [40], a single slot recurrence along frequency network (SisRafNet), a recurrent neural network (RNN)-based method, was introduced that captures frequency-domain correlations between subcarriers for improved channel estimation in OFDM systems. Simulation results showed superior performance over the LMMSE method and other DL models across various SNR levels. [41] proposed a self-normalizing convolutional bidirectional gated recurrent unit network (SCBiGNet), a DL-based framework that combined a self-normalizing network (SNN), CNN, and bidirectional gated recurrent unit (BiGRU) for OFDM channel estimation and signal detection. The method improved estimation stability and achieved lower BER compared to LS, bidirectional LSTM (BiLSTM), and gated recurrent unit (GRU)-based models. Robustness was observed in scenarios with limited pilots and short cyclic prefixes. While these architectures achieved superior performance, their complexity limited real-time implementation in resource-constrained environments. Specialised techniques have been developed for specific MIMO configurations and frequency division systems, offering targeted solutions but with limited generalisability across different system architectures. In [42], a complex residual denoising convolutional neural network (CR-DnCNN) was introduced for frequency division duplexing (FDD) MIMO channel estimation. The method combined compressive sensing with DL-based denoising to improve estimation accuracy while reducing pilot overhead. Simulation results showed lower NMSE and BER compared to LS and orthogonal matching pursuit (OMP). In [43], an involution-based channel estimation (InvoEsNet) was introduced for OFDM channel estimation under time-varying channels. This method applied a modified involution-based preprocessing subnetwork (ResCSINet) to mitigate inter-carrier interference (ICI) and a residual CSI subnetwork (ResCSINet) for further refinement. Simulation results showed improved NMSE performance compared to other conventional and DL-based benchmarks. These specialised approaches excelled in their target scenarios but required significant modification for different system configurations. Building on these developments, ML models have been designed specifically for NOMA or RIS environments. For NOMA, a convolutional neural network (CNN)-based channel estimation model was developed for mmWave massive MIMO-NOMA systems in [33]. The proposed model improved estimation accuracy over the conventional least squares (LS) estimator and the Cramer-Rao bounds (CRB) approach. A hybrid deep learning (DL) approach was introduced in [44] for channel estimation and power allocation in multiple-input single-output (MISO)-NOMA systems. This approach integrated long short-term memory (LSTM) networks for predicting channel coefficients and employed CNNs for optimizing power allocation. The proposed approach demonstrated superior performance compared to conventional methods such as minimum mean square error (MMSE) for channel estimation and fixed power allocation strategies. While these NOMA-specific approaches address power-domain multiplexing challenges, they have not

been extensively validated in RIS-enhanced environments. Channel estimation for RIS-aided systems presents unique challenges due to the cascaded channel structure and increased dimensionality, leading to innovative solutions that balance estimation accuracy with computational feasibility. To address this, a learning-based approach was introduced in [29] for channel estimation in RIS-assisted downlink massive MIMO systems. The proposed method utilised a deep neural network (DNN) at the user equipment to estimate effective downlink channel gains. Simulation results demonstrated that the learning-based approach achieved lower normalized mean square error (NMSE) compared to the hardening bound and model-based approaches. However, these initial RIS approaches primarily focus on isolated RIS deployment without considering integration with advanced multiple access schemes. Advanced ML frameworks have been developed to address the complexity of RIS-aided channel estimation, though they often face scalability challenges when extended to large-scale deployments. [45] introduced a distributed machine learning (DML) framework for downlink channel estimation in RIS-aided systems. Additionally, a DML-based hierarchical neural network architecture was developed to enhance estimation accuracy by classifying different channel scenarios before extracting relevant features. Simulation results showed that this method outperformed conventional LS and MMSE-based approaches while significantly reducing pilot overhead. A global attention residual network (GARN) was presented in [46] for channel estimation in mmWave RIS-assisted single-input multiple-output (SIMO) systems. The method applied a global attention mechanism for multi-channel feature fusion and a residual learning module to enhance estimation accuracy. A unit cell grouping strategy reduced pilot overhead, and GARN reconstructed the complete channel matrix from the grouped estimates. Simulation results showed lower NMSE compared to interpolation and super-resolution-based methods. In [30], a residual neural network (InterpResNet) was developed for cascaded channel estimation in a RIS-aided MIMO system. Compared to other approaches, such as residual channel estimation network (ReEsNet), transformer-based models, and bilinear alternating least squares (BALS), InterpResNet achieved lower NMSE while maintaining a simpler network structure. While these frameworks show promise, their performance in dynamic environments with varying RIS configurations remains largely unexplored. Furthermore, joint channel estimation and CSI feedback techniques have also been explored for RIS-assisted systems, offering integrated solutions but with increased implementation complexity. A joint DL-based channel estimation and feedback network (JDCNet), a DL-based framework, was proposed in [47] for joint channel estimation and CSI feedback in RIS-assisted communication systems. JDCNet integrated preliminary channel estimation with errors into the feedback process to minimize cumulative errors. A pilot grouping strategy reduced overhead while maintaining high CSI reconstruction accuracy. Simulation results demonstrated superior performance compared to other DL-based and compressive sensing-based methods. These joint approaches provide comprehensive solutions but require careful design to balance estimation accuracy with feedback overhead. While the majority of studies have focused on NOMA or RIS in isolation, a few recent studies have begun to tackle the joint RIS-NOMA channel estimation problem using classical deep learning models. These works represent the current state-of-the-art. However, the immense complexity and high dimensionality inherent in the joint RIS-NOMA environment continue to pose significant scalability and performance challenges for classical ML architectures. This difficulty in finding efficient classical solutions motivates the exploration of new computational paradigms, such as QML, that may be better suited to such complex problems. Channel estimation represents a critical yet underexplored application area for quantum computing in wireless communications, with existing approaches demonstrating theoretical potential but lacking comprehensive solutions for complex multi-user scenarios with advanced surface technologies. In the context of quantum algorithms for channel estimation, [36] explored the application of quantum computing algorithms in massive MIMO mmWave systems. The study focused on amplitude encoding for channel estimation at the physical layer of transceivers. This highlighted the potential for exponential computational efficiency gains that quantum methods can offer. Furthermore, [37] introduced a modular QML framework for wireless channel estimation in simultaneously transmitting and reflecting reconfigurable intelligent surface (STAR-RIS)-aided communication systems. This framework incorporated distinct quantum learning modules that effectively eliminated noise and accurately estimated channels for devices operating in both reflection and transmission regions. Their approach demonstrated the efficiency of quantum techniques in complex RIS-aided environments. While quantum-based methods showed significant promise in addressing computational challenges, their application in channel estimation has not been extensively studied. Most existing studies have focused on classical and ML techniques. While these methods are effective, they often face challenges with scalability and computational complexity in high-dimensional and dynamic wireless systems with various configurations. This highlights the necessity for further investigation into quantum-driven approaches to fully unlock their potential in wireless communications.

B. RIS-aided 6G NOMA Systems

The integration of RIS and NOMA has been widely studied for improving system performance in next-generation wireless networks, with the literature progressing from fundamental system designs to advanced multi-RIS configurations and specialised applications. Early studies focused on establishing the basic integration principles and demonstrating performance gains over conventional approaches, though these initial studies primarily considered simplified scenarios with perfect channel conditions. [48] proposed a RIS-enabled downlink NOMA system, where RIS partitions perform over-the-air modulation to serve multiple users. Unlike conventional NOMA, which applied superposition coding at the base station (BS) or receiver, the proposed approach enabled RIS to modulate and reflect signals with distinct phase shifts for different users. Closed-form expressions for outage probability

and BER were derived under both perfect and imperfect CSI conditions. Simulation results demonstrated that RIS-enabled downlink NOMA outperformed OMA in terms of sum rate and spectral efficiency, particularly in scenarios with high quality-of-service (QoS) constraints. In [49], a RIS-assisted hybrid NOMA (HNOMA) system (PR-HNOMA) was proposed to improve spectral and energy efficiency. The system utilised joint beamforming at the BS and RIS, optimised through semi-definite relaxation (SDR) and alternating optimization (AO) techniques. Simulation results demonstrated that PR-HNOMA outperformed conventional RIS-assisted NOMA (R-HNOMA), RIS-assisted NOMA (R-CNOMA), and RIS-assisted OMA (R-OMA), even under imperfect SIC (ISIC). In [50], the performance of RIS-aided coordinated NOMA (C-NOMA) systems was analysed by deriving closed-form and asymptotic expressions for outage probability (OP) and ergodic capacity (EC). The study considered discrete phase-shift alignment at RIS and ISIC to evaluate practical system performance. An increased number of RIS elements was shown to improve OP and EC. The simulation results also confirmed that RIS-assisted C-NOMA outperformed conventional OMA and non-RIS-assisted C-NOMA systems. While these foundational works established the viability of RIS-NOMA integration, they primarily relied on theoretical analysis with limited consideration of practical implementation challenges such as real-time RIS control and channel estimation complexity. Research efforts have evolved towards sophisticated RIS deployments that address scalability and coverage limitations, though these advanced configurations introduce significant complexity in optimisation and coordination. [51] investigated a secure transmission strategy for STAR-RIS-assisted NOMA-ISAC systems and formulated a sum secrecy rate maximisation problem. The study optimised transmit beamforming, artificial jamming, and STAR-RIS passive beamforming while maintaining the required beampattern gain for sensing targets. To address the non-convex nature of the problem, an alternating optimization algorithm based on successive convex approximation (SCA) was developed. Simulation results showed that STAR-RIS improved security in NOMA-based ISAC networks by reducing eavesdropping threats while enhancing both communication and sensing performance. Multi-cell NOMA systems assisted by multiple RIS with inter-RIS reflection were studied in [52] to minimise total transmit power. Unlike previous works that focused on single-RIS or non-interacting RIS deployments, this study considered RIS placement near both BSs and edge users. A new NOMA scheme based on inter-group interference cancellation (IGIC) was presented to reduce interference from central users to edge users. Simulation results showed that the proposed multi-reflection RIS with IGIC-based NOMA achieved lower transmit power compared to conventional RIS-NOMA strategies. [53] investigated a multi-carrier (MC)-NOMA system assisted by RIS and proposed a competitive RIS-assignment strategy to optimise resource allocation while ensuring QoS constraints. A sequential convex approximation algorithm was applied to address the non-convex nature of the optimisation problem, achieving a sub-optimal solution. Simulation results demonstrated that the proposed RIS-assignment method achieved lower transmit power compared to random RIS allocation while maintaining QoS requirements. These advanced configurations offered enhanced performance and coverage but faced practical challenges including increased signalling overhead, complex coordination algorithms, and higher computational requirements for real-time optimisation. Recent developments have explored RIS-NOMA integration in specialised scenarios, which demonstrated versatility but often required application-specific solutions that limit generalisability. A multi-user NOMA system integrated with multiple RIS was investigated in [54] to facilitate backscatter communication (BC) in a symbiotic cognitive radio network (CRN). A joint resource allocation problem was formulated to optimise power allocation, RIS reflection coefficients, and interference cancellation, to maximise the sum rate of both primary and secondary networks. A weighted MMSE (WMMSE) method was applied to transform the complex optimisation problem into a convex one, which allowed an iterative algorithm to find an optimal solution. Simulation results demonstrated that the proposed approach outperformed conventional NOMA and RIS-based systems. In [55], convert MEC in RIS-aided NOMA systems was analysed. The study derived closed-form expressions for the minimum detection error probability (DEP) and ergodic covert/public rates, which served as a theoretical foundation for evaluating covert communication performance. A reinforcement learning (RL)-based power allocation algorithm was introduced to optimise transmit and jamming power, which improved both security and communication efficiency. Simulation results demonstrated that the RL-based approach improved covert communication reliability compared to the baseline Q-learning-based power allocation scheme. In [56], a multi-user NOMA system enhanced by aerial RIS mounted on unmanned aerial vehicles (UAVs) was introduced to improve coverage and spectral efficiency. A joint optimisation problem was formulated to maximize the sum rate by optimising UAV positioning, RIS reflection coefficients, and power allocation. A successive convex approximation (SCA) approach combined with semi-definite programming (SDP) was applied to solve the non-convex problem, leading to a sub-optimal solution. Simulation results demonstrated that the proposed aerial RIS-NOMA system outperformed fixed RIS-NOMA and OMA-aerial RIS systems in terms of sum rate and energy efficiency. While these specialised applications showcased the flexibility of RIS-NOMA systems, they often required tailored optimisation algorithms and might not translate effectively to other deployment scenarios. Cutting-edge studies have explored advanced RIS technologies and hybrid configurations, which achieved superior performance but introduced new technical challenges in terms of hardware complexity and energy consumption. A holographic RIS (HRIS)-assisted THz NOMA system was investigated in [57] to improve spectral efficiency and outage performance. Closed-form OP expressions were derived under both perfect SIC and imperfect SIC conditions, along with an asymptotic high-SNR analysis. Simulation results demonstrated that HRIS-assisted THz-NOMA outperformed conventional OMA while highlighting the negative impact of beam misalignment on system reliability. In [58], a RIS-assisted unified NOMA (U-NOMA) framework was presented, which integrates both power-domain NOMA (PD-

NOMA) and code-domain (CD-NOMA) to enhance system performance. Closed-form expressions for OP and ergodic rate were derived under both perfect SIC and imperfect SIC conditions. Simulation results demonstrated that RIS-U-NOMA achieved better outage behaviour, higher ergodic rates, and improved system throughput compared to RIS-OMA and decode-and-forward (DF) relay systems. [59] investigated a double RIS-assisted NOMA system, integrating both passive RIS (PRIS) and active RIS (ARIS) to enhance system performance. Closed-form and asymptotic expressions were derived for outage probability and ergodic data rate under perfect SIC and imperfect SIC conditions. Simulation results demonstrated that PRIS-ARIS-NOMA outperformed PRIS-ARIS-OMA and double PRISs-NOMA, particularly in low-transmit power scenarios. The study also showed that increasing the number of reflecting elements improved outage performance, ergodic data rate, and system throughput. In [60], the secrecy performance of multi-functional RIS (MF-RIS)-assisted NOMA networks was analysed considering both external and internal eavesdropping scenarios. The study derived closed-form and asymptotic expressions for the secrecy outage probability (SOP) and secrecy throughput under the effects of receiver hardware impairments and imperfect SIC. Numerical results showed that MF-RIS outperformed active RIS and STAR-RIS in secrecy performance under the same power budget. At high power levels, residual interference from imperfect SIC was identified as the dominant factor limiting secrecy capacity and exceeding the impact of thermal noise. The findings also revealed that deploying more MF-RIS elements significantly enhanced secrecy against external eavesdroppers but had a limited effect against internal eavesdroppers. These findings suggested that power allocation and interference mitigation strategies are crucial in enhancing the secrecy performance of MF-RIS-assisted NOMA networks. These advanced technologies demonstrate significant performance improvements but face substantial implementation barriers including increased hardware costs, complex control mechanisms, and higher energy consumption, particularly for active RIS components. Channel estimation in RIS-NOMA represents a critical yet underexplored area, with existing approaches showing promise but lacking comprehensive solutions for the unique challenges posed by cascaded channel structures and multi-user interference. [34] proposed a DL-based approach using a combined CNN-LSTM model. This approach demonstrated robustness across different system parameters, such as signal-to-noise ratio (SNR), power allocation factor, and the number of RIS elements. Additionally, the simulation results showed that the proposed model outperformed other benchmark models in terms of different evaluation metrics. Similarly, a ML-based approach was introduced in [35] to perform joint channel estimation and signal detection in a RIS-NOMA network that provides efficient mitigation of SIC error propagation. The proposed framework leveraged a four-layer DL model with an LSTM core structure. The simulation results demonstrated significant improvements in both channel estimation and signal detection when using the LSTM-based model compared to conventional LS and MMSE methods. Although a few studies have addressed this topic, channel estimation for RIS-NOMA systems still receives limited attention in the existing literature. This limitation is particularly concerning given that accurate CSI is essential for realising the theoretical benefits of RIS-NOMA integration, highlighting the need for more sophisticated and computationally efficient channel estimation techniques.

C. Quantum Technologies for 6G

Quantum technologies have emerged as a promising solution to address the growing computational and communication challenges in 6G wireless networks, progressing from fundamental security applications to sophisticated learning frameworks. These techniques, including quantum-inspired machine learning methods [21] and quantum-inspired optimisation techniques [61], enhance resource management, security optimisation, spectrum allocation, interference mitigation, and real-time decision-making in dynamic and complex network environments [62]. Early quantum applications in 6G networks have focused on security enhancement through quantum key distribution and quantum communication protocols, which demonstrated strong theoretical foundations but faced significant deployment challenges due to infrastructure requirements and distance limitations. In [63], a quantum-secured space-air-ground integrated network (Q-SAGIN) that applied quantum key distribution (QKD) was introduced to strengthen security in 6G networks. The study introduced a universal QKD service provisioning framework, which incorporated optical fiber-, satellite-, and UAV-based QKD to establish secure key distribution across different network layers. A stochastic programming model was developed to optimise QKD service allocation while balancing cost efficiency and security. A metaverse-based case study evaluated the proposed framework and confirmed its potential for secure and scalable quantum communications in future 6G applications. A privacy-preserving resource allocation framework for federated edge learning (FEL) in the quantum internet was proposed in [64], which incorporated QKD and multi-agent reinforcement learning to improve security and efficiency. A Stackelberg game model was formulated to optimise secure communication and data resource allocation, while a partially observable Markov decision process (POMDP) enabled intelligent decision-making. The proposed multi-agent federated reinforcement learning approach improved policy convergence and mitigated security risks by avoiding direct information sharing. Experimental results showed that the proposed approach outperformed baseline methods in cost efficiency and security. In [65], two full-duplex quantum communication protocols, quantum duplex coding and quantum telexchanging, were proposed, which enabled simultaneous bidirectional transmission of classical and quantum information without physically transferring particles. Quantum duplex coding allowed two-way classical information transmission using a single pre-shared Bell pair, while quantum telexchanging facilitated the exchange of unknown quantum states without pre-shared entanglement. The study modelled these protocols as binary and quantum erasure channels, and their feasibility was evaluated by deriving capacity-achieving distributions and theoretical performance

limits. Analytical results showed that these protocols achieved full-duplex quantum communication with reliable information transfer and provided insights into channel capacities and operational constraints under various quantum erasure conditions. While these security-focused approaches provided theoretically unbreakable communication, they required sophisticated quantum infrastructure and are vulnerable to practical implementation imperfections, limiting their immediate deployment in commercial 6G networks. Recent developments have integrated quantum computing principles with ML to address complex optimisation problems in 6G networks, which achieved significant performance improvements but required careful design to balance quantum advantages with classical processing capabilities. In [66], a quantum-enhanced federated learning (FL) framework named QV-FEDCOM was introduced for metaverse-empowered vehicular networks, which addressed challenges such as high communication costs, data heterogeneity, and memory constraints. The framework incorporated quantum sequential training program (Q-STP) to optimise communication efficiency, quantum vehicular context grouping (Q-VCG) for managing heterogeneous data, and quantum-inspired principal component analysis (Q-PCA) for reducing memory usage. A novel quantum trajectory loss (QTL) function was also introduced to enhance trajectory prediction accuracy by integrating Huber loss and an angular deviation penalty. Simulation results demonstrated that QV-FEDCOM significantly reduced communication overhead while improving learning efficiency in vehicular networks. A deep quantum-transformer network (QTN) framework was proposed in [67] for multimodal beam prediction in ISAC systems. The framework integrated quantum embeddings with vision transformers (ViTs) and CNNs to enhance learning efficiency and feature representation. Evaluation using the DeepSense 6G dataset showed improvements in beam selection accuracy and zero-shot generalisation over conventional deep learning-based methods. Simulation results demonstrated that quantum-enhanced multimodal learning effectively reduced beam training overhead while improving adaptability in dynamic environments. These quantum-enhanced learning approaches demonstrated significant computational advantages and improved convergence properties, but their performance gains were often dependent on specific problem structures and might not translate uniformly across all network optimisation scenarios. Advanced quantum-enhanced reinforcement learning frameworks have been developed to tackle complex resource allocation and task offloading problems, showing superior performance in high-dimensional decision spaces but facing scalability challenges when transitioning from simulation to real-world deployment. In [68], a quantum-enhanced deep reinforcement learning (DRL) framework was presented for direction-of-arrival (DoA) estimation and task offloading in ISAC systems. The framework integrated quantum-enhanced actor-critic learning to improve learning efficiency and decision-making accuracy, while overcoming the limitations of traditional DRL methods in high-dimensional state spaces. Simulation results demonstrated up to 91.66% improvement in DoA estimation accuracy and 43.09% reduction in task offloading latency compared to conventional DRL-based approaches. A quantum-aided deep reinforcement learning (Quantum-DRL) framework was proposed in [69] for task offloading in vehicular edge computing (VEC) networks. The model integrated digital twins (DTs) and long short-term memory (LSTM) networks to enhance real-time decision-making. A Nash equilibrium-based multi-agent DRL model was introduced to optimise task scheduling among vehicles, UAVs, and BSs. Simulation results demonstrated that the proposed Quantum-DRL framework achieved better task offloading efficiency and lower latency compared to conventional DRL-based approaches. While these quantum DRL frameworks achieved remarkable performance improvements in controlled environments, they faced significant challenges in terms of quantum noise tolerance, limited qubit availability, and the need for error correction mechanisms that might offset computational advantages in near-term quantum devices.

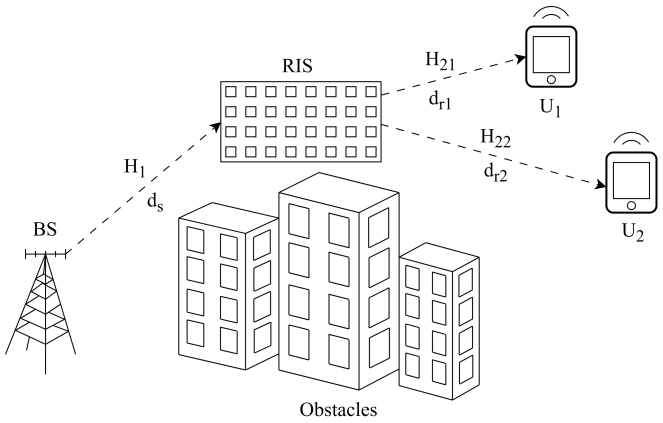

Fig. 1: System model of the considered downlink RIS-NOMA communication scenario.

IV. System Model and Problem Formulation

This paper considers a downlink communication scenario in a RIS-NOMA system, which consists of an S-antenna BS, a R-element RIS, and K users with Q antennas each as shown in Fig. 1. The direct communication path from BS to user U_k, where $k \in \{1, 2, \ldots, K\}$, is obstructed. Each user U_k receives its signal from the BS through the indirect path via RIS: $BS \rightarrow RIS \rightarrow U_k$. At each time step t, user U_k is assumed to move farther from the BS with a constant speed v, which is sufficiently slow to prevent the occurrence of Doppler effects. It is assumed that all channels experience Rayleigh fading. Throughout this paper, all channels are assumed to remain relatively unchanged within a channel coherence block, which has a duration (coherence time) of T_c on the order of tens milliseconds (ms). At each time step $t = 1, 2, \ldots, T_c$, the cascaded channel from $BS \rightarrow RIS \rightarrow U_k$, denoted by $\mathbf{C}_k$, is calculated as follows:

$$\mathbf{C}_k(t) = \mathbf{H}_{2k}^{\dagger}(t)\mathbf{\Phi}(t)\mathbf{H}_1(t), \tag{1}$$

where $\mathbf{H}_{2k}(t) \in \mathbb{C}^{R\times Q}$ and $\mathbf{H}_1(t) \in \mathbb{C}^{R\times S}$ represent the channel matrices of the links $RIS \rightarrow U_k$ and $BS \rightarrow RIS$, respectively. The $\mathbf{\Phi}(t) = [\kappa_1 e^{j\varphi_1(t)}, \kappa_2 e^{j\varphi_2(t)}, \ldots, \kappa_R e^{j\varphi_R(t)}]^T$ is the diagonal reflection matrix of RIS, where $\varphi_r \in [0, 2\pi]$ is

the phase shift and κ_r is the amplitude reflection coefficient. Given the BS transmit power P_t and power allocation factor assigned to U_k, denoted by ζ_k, where $\sum_{k=1}^{K} \zeta_k^2 = 1$ and $\zeta_1 < \zeta_2 < \ldots < \zeta_K$, the BS transmits to all users a superposed signal $x(t) = \sqrt{P_t} \sum_{k=1}^{K} \zeta_k x_k(t)$, where $x_k(t) \in \mathbb{C}^{S\times 1}$. At time step t, the received signal at U_k is given by

$$y_k(t) = \sqrt{L_k(t)}\mathbf{C}_k(t)\rho\frac{x(t)}{\sqrt{P_t}} + \eta_k(t), \tag{2}$$

where $L_k(t) = L_s L_{rk}(t)$ is the path loss parameter at U_k. L_s and L_{rk} are the path loss factors from BS to RIS and from RIS to U_k, respectively. The path loss is a distance-dependent parameter and is defined as $L(\widehat{d}) = (\widehat{d}/d_0)^{-\tau}$ where $\widehat{d}$ is the path link distance, d_0 is a reference distance, and the path loss exponent (PLE) of the environment is defined by τ [70]. In (2), $\eta_k(t) \in \mathbb{C}^{Q\times 1}$ is the zero-mean complex additive white Gaussian noise (AWGN) with variance $N_0 = 1$ at U_k and $\rho = P_t/N_0$ is the SNR. Upon receiving the superimposed signal, each user applies SIC to decode their intended signal following the NOMA principle. NOMA allows all users to share the same time and frequency resources by transmitting signals with different power levels. The BS allocates higher power to users with weaker effective channel gains and lower power to users with stronger effective channel gains. Each user with a stronger effective channel gain decodes and cancels the signals intended for weaker users before decoding their own signal. In general, this process requires full knowledge of the CSI for all cascaded channels, which is not a practical assumption. Using this CSI, SIC successively cancels higher-power signals until the desired signal is retrieved. For user k, the decoded signal x_k has the corresponding signal-to-interference-plus-noise ratio (SINR) given by

$$\varepsilon_k = \frac{|\widehat{h}_k|^2 P_t(\zeta_k)^2}{\sum_{i=1}^{k-1} |\widehat{h}_i|^2 P_t(\zeta_i)^2 + N_0}, \tag{3}$$

where $\widehat{h}_k = \sqrt{L_k}\mathbf{C}_k$ with $k = 1, 2, \ldots, K$ [71]. In this RIS-NOMA scenario, the channel between the BS and the RIS remains unchanged, whereas the channels between the RIS and the users are considered slowly time-varying, as users move progressively farther from the BS at a constant speed. Prior knowledge of the cascaded channel gains from $BS \rightarrow RIS \rightarrow U_k$ is essential to implement SIC at the receiver. In this work, the received signals at the users are used to estimate the cascaded channels, as the RIS functions only as a signal reflector. The gradual movement of the users causes the cascaded channels to gradually change, resulting in a time-varying channel estimation problem in the RIS-NOMA system. Following the dataset generation algorithm in [34], we generate datasets for various system configurations to evaluate our proposed model. Each dataset contains D samples, where each sample is equivalent to a time step t in the RIS-NOMA system. The channel gains $\mathbf{H}_1$ and $\mathbf{H}_{2k}$, and the signal x_k at U_k are assumed to be independent and follow complex Gaussian distributions. For each configuration, we generate the received signals at all users, denoted by $\mathbf{Y} \in \mathbb{C}^{D\times QS\times K}$, and the corresponding cascaded channels from $BS \rightarrow RIS \rightarrow U_k$, denoted by $\mathbf{C} \in \mathbb{C}^{D\times QS\times K}$,

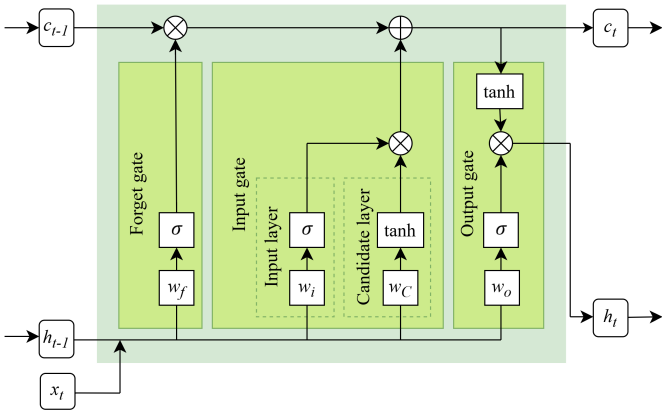

Fig. 2: The structure of an LSTM cell.

which serve as the input and output of the model, respectively. Before feeding the data into the QML model, preprocessing is performed. The received signals at all users are expressed as a time series, $\mathbf{Y} = [\mathbf{Y}(1), \mathbf{Y}(2), \ldots, \mathbf{Y}(D)]$, where $\mathbf{Y}(t) = [y_1(t), y_2(t), \ldots, y_K(t)]$ and $y_k(t) \in \mathbb{C}^{Q\times S}$ for each time step $t \in [1, 2, \ldots, D]$. The received signal at user U_k, denoted by $y_k(t)$, is a complex matrix, which cannot be directly input into the QML model. Therefore, for each $y_k(t)$, its magnitude and phase are calculated and concatenated into a single dimension. As a result, the dimension of the data for a single user is transformed to $y_k(t) \in \mathbb{R}^{2\times Q\times S}$, and the full input tensor becomes $\mathbf{Y} \in \mathbb{R}^{D\times K\times 2QS}$. A similar process is repeated to the cascaded channels $BS \rightarrow RIS \rightarrow U_k$, denoted by $\mathbf{C} = [\mathbf{C}(1), \mathbf{C}(2), \ldots, \mathbf{C}(D)]$, where $\mathbf{C}(t) = [C_1(t), C_2(t), \ldots, C_K(t)]$. For each $C_k(t)$, the magnitude is calculated. The magnitudes and phases of the received signals are taken as input features, while the magnitudes of the cascaded channels are taken as the output. Before being fed into the proposed model, $\mathbf{Y}(t)$ and $\mathbf{C}(t)$ are converted into sequences of t_1 time steps. The dataset length is then changed and denoted by D'.

V. Proposed Model

This section provides a detailed description of the QML model proposed for channel estimation in a 6G RIS-NOMA integrated system.

A. Quantum Long Short-Term Memory

The LSTM model, a particular type of RNN, was developed to handle the challenges of capturing long-term dependencies in sequential data [72]. LSTMs mitigate the problems of vanishing and exploding gradients that are common in traditional RNNs. In contrast to RNNs, LSTMs can preserve long-term information through a structured cell state update process, which has been proved beneficial for tasks involving sequential data such as NLP and time-series forecasting. The LSTM architecture consists of one or a sequence of memory cells, each equipped with three primary components: a forget gate, an input gate, and an output gate, which work together to manage the cell state. The structure of an LSTM cell is shown in Fig. 2. In the LSTM architecture, c_t represents the cell state

at time step t. It serves as the memory component that carries forward information across different time steps, allowing the network to retain long-term dependencies in sequential data. The cell state c_t is updated using a combination of the input gate, forget gate, and output gate, with contributions from the current input x_t and the hidden state h_{t-1} from the previous time step. In contrast to RNNs, which rely exclusively on the hidden state h_t for memory retention, LSTMs incorporate both h_t and c_t as distinct memory components. The symbols $\otimes$ and $\oplus$ respectively represent element-wise multiplication and addition. The mathematical formulation of an LSTM cell is given by the following set of equations

$$
\begin{aligned}
f_t &= \sigma(w_f \cdot [h_{t-1}, x_t] + b_f) \\
i_t &= \sigma(w_i \cdot [h_{t-1}, x_t] + b_i) \\
C_t &= \tanh\left(w_C \cdot [h_{t-1}, x_t] + b_C\right) \\
o_t &= \sigma(w_o \cdot [h_{t-1}, x_t] + b_o) \\
c_t &= f_t \cdot c_{t-1} + i_t \cdot C_t \\
h_t &= o_t \cdot \tanh(c_t),
\end{aligned} \tag{4}
$$

where σ represents the sigmoid function, $\tanh$ represents the hyperbolic tangent activation function, and w_f, w_i, w_C, and w_o denote the weight parameters corresponding to the forget gate, input gate, candidate cell state, and output gate, respectively. Similarly, b_f, b_i, b_C, and b_o are the associated bias parameters. All these parameters are updated during the training process. The forget gate outputs the vector f_t that decides which parts of the previous cell state c_{t-1} should be retained or discarded. The input gate decides which new information should be added to the cell state c_t. This gate consists of two layers: the input gate layer and the candidate layer. The input layer produces a vector i_t that determines which elements of the candidate cell state update C_t should be added to the cell state c_t. The output gate o_t controls what information from the cell state is used to update the hidden state h_t, which is then passed to the next time step. The structure of the QLSTM, shown in Fig. 3, is built upon the traditional LSTM, replacing the internal neural network components within the LSTM cell with VQCs. To align the input dimension with the number of qubits in the VQC block, a linear layer first transforms the concatenated input vector $[h_{t-1}, x_t]$. The transformed vector is then passed through four independent VQCs, each responsible for computing one of the LSTM gate functions. Each VQC output is processed by a corresponding linear layer to match the required hidden state dimension of the QLSTM cell. The data flow within the QLSTM cell is mathematically formulated as:

$$
\begin{aligned}
z_t &= L_{in}\{[h_{t-1}, x_t]\} \\
f_t &= \sigma\{L_{out_1}[VQC_1(z_t)]\} \\
i_t &= \sigma\{L_{out_2}[VQC_2(z_t)]\} \\
C_t &= \tanh\{L_{out_3}[VQC_3(z_t)]\} \\
o_t &= \sigma\{L_{out_4}[VQC_4(z_t)]\} \\
c_t &= f_t \cdot c_{t-1} + i_t \cdot C_t \\
h_t &= o_t \cdot \tanh(c_t),
\end{aligned} \tag{5}
$$

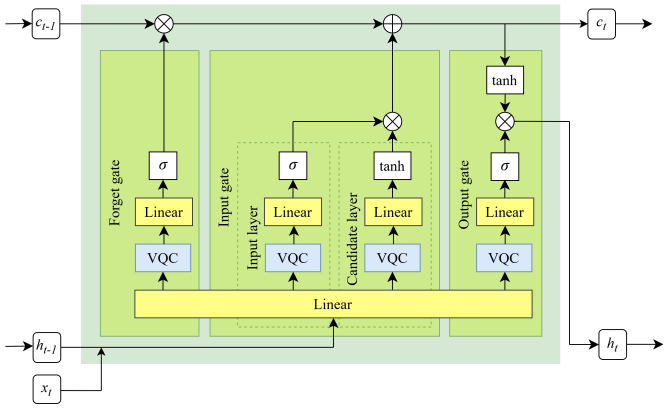

Fig. 3: The structure of a QLSTM cell.

where L_{in} denotes the input linear transformation, VQC_i represents the i-th variational quantum circuit, and L_{out_i} is the linear layer applied after each VQC_i to match the hidden state dimension.

B. Variational Quantum Circuit

A VQC is a parametrised quantum circuit that uses classical optimisation methods to adjust its internal parameters to minimise a predefined cost function. A VQC is composed of three primary components: a data embedding layer, a variational layer, and a measurement layer. The data embedding layer serves as the interface between classical and quantum information by encoding classical data into quantum states. This process relies on two key quantum principles. First, superposition allows each qubit to represent a combination of multiple values simultaneously, rather than a single binary 0 or 1. Second, this property enables quantum parallelism, where a single gate operation can act on all of these possibilities at once. This allows the circuit to work within a high-dimensional feature space, which provides a potential advantage over classical models where creating such expressive feature representations can require much deeper networks or manual feature engineering. In the context of channel estimation, this means a single quantum state can represent a rich combination of potential channel conditions based on the received signal features, allowing the model to explore a vast solution space efficiently. A quantum state is mathematically described as a vector in a complex Hilbert space. For a single qubit, the quantum state can be expressed as $|\xi\rangle = \mu|0\rangle + \nu|1\rangle$. Unlike a classical bit that is restricted to a state of either 0 or 1, the state of a single qubit is defined by two continuous complex amplitudes (μ and ν), allowing it to hold a significantly richer combination of information. The squared magnitudes of these coefficients, $|\mu|^2$ and $|\nu|^2$, represent the probability of measuring the qubit in either the $|0\rangle$ or $|1\rangle$ state, respectively, and must sum to one (i.e., $|\mu|^2 + |\nu|^2 = 1$). This inherent probabilistic and high-dimensional nature gives VQCs a powerful mechanism for encoding and manipulating data that has no direct classical counterpart. The structure of the data embedding layer used in this paper is shown in Fig. 4. The initial quantum state of

the circuit, consisting of N qubits, can be written as

$$|0\rangle \otimes |0\rangle \otimes \cdots \otimes |0\rangle = |00\cdots 0\rangle = |0\rangle^{\otimes N}, \tag{6}$$

which corresponds to a column vector of dimension $2^N \times 1$, with only the first entry equal to one and the rest zero:

$$|0\rangle^{\otimes N} = \begin{bmatrix} 1 \\ 0 \\ 0 \\ \vdots \\ 0 \end{bmatrix}. \tag{7}$$

To map this initial state to a superposition state, a Hadamard gate H is applied to each qubit. Conceptually, the Hadamard gate creates quantum superposition, which can be understood with the analogy of a spinning fair coin. While in motion, the coin is not in a definite state of heads or tails but in a combination of both. This represents quantum superposition. Similarly, the Hadamard gate places each qubit into a superposition of $|0\rangle$ and $|1\rangle$ states, enabling the quantum system to process multiple possibilities simultaneously, a task that would require a classical system to handle each possibility sequentially. This simultaneous processing is particularly useful for channel estimation, as the model can effectively evaluate many different hypotheses about the complex and time-varying behaviour of the channel in a single computational step. This parallel processing capability is a fundamental aspect of the potential computational advantages of quantum computing. The Hadamard gate transforms the basis states as follows:

$$\begin{aligned} H : |0\rangle &\rightarrow \frac{1}{\sqrt{2}}\left(|0\rangle + |1\rangle\right), \\ |1\rangle &\rightarrow \frac{1}{\sqrt{2}}\left(|0\rangle - |1\rangle\right). \end{aligned} \tag{8}$$

Mathematically, this quantum mechanical property is expressed in matrix form as

$$H = \frac{1}{\sqrt{2}} \begin{bmatrix} 1 & 1 \\ 1 & -1 \end{bmatrix}. \tag{9}$$

Applying the Hadamard gate to each qubit in the $|0\rangle^{\otimes N}$ state produces

$$\begin{aligned} |\chi_1\rangle &= H^{\otimes N} |0\rangle^{\otimes N} \\ &= \bigotimes_{n=1}^{N} \frac{1}{\sqrt{2}} \left(|0\rangle + |1\rangle\right) = \frac{1}{\sqrt{2^N}} \sum_{q=0}^{2^N-1} |q\rangle. \end{aligned} \tag{10}$$

Here, $|q\rangle$ represents all possible N-bit binary states, ranging from $|000\ldots0\rangle$ when $q = 0$ to $|111\ldots1\rangle$ when $q = 2^N - 1$. After applying the Hadamard gate to transform the initial quantum state into a superposition state, classical data are introduced into the quantum circuit. Specifically, each element of the N-dimensional classical input vector $\overrightarrow{u} = (u_1, u_2, \ldots, u_N)$ is used to generate rotation angles that encode the data into the quantum state. For each element u_n, we generate angles $\psi_{n,1} = \tan^{-1}(u_n)$ and $\psi_{n,2} = \tan^{-1}(u_n^2)$. The arctan function ensures the angles are bounded within $(-\pi/2, \pi/2)$, which helps maintain numerical stability and prevents extreme values of u_n from skewing the rotations.

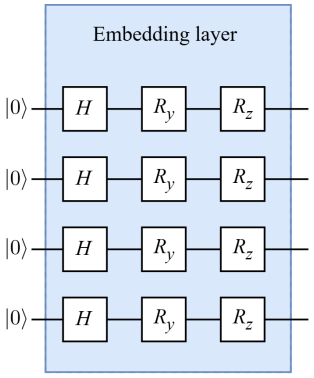

Fig. 4: The structure of the data embedding layer.

Additionally, u_n^2 is used to capture higher-order features, enriching the representation of classical data in the quantum domain. This ability to encode non-linear transformations of features directly into quantum states provides a compact method for enriching the feature space of the model, a task that might otherwise require additional layers in a classical network. The quantum state is then transformed by applying sequential R_y and R_z rotation gates to each qubit using the generated angles $\psi_{n,1}$ and $\psi_{n,2}$:

$$|\chi_2\rangle = \bigotimes_{n=1}^{N} R_z\left(\psi_{n,2}\right) R_y\left(\psi_{n,1}\right) |\chi_1\rangle, \tag{11}$$

where $R_y(\vartheta)$ rotates the qubit around the y-axis of the Bloch sphere. Its matrix representation can be defined as

$$R_y(\vartheta) = \begin{bmatrix} \cos(\vartheta/2) & -\sin(\vartheta/2) \\ \sin(\vartheta/2) & \cos(\vartheta/2) \end{bmatrix}. \tag{12}$$

Similarly, rotation gate $R_z(\vartheta)$ rotates a qubit around the z-axis of the Bloch sphere. Its matrix representation is shown as

$$R_z(\vartheta) = \begin{bmatrix} e^{-i\vartheta/2} & 0 \\ 0 & e^{i\vartheta/2} \end{bmatrix}. \tag{13}$$

The variational layer is the central learning component of the circuit, where the expressive power of the model is developed. It is composed of two types of operations that serve distinct but complementary functions. First, entangling gates, such as controlled-NOT (CNOT), controlled-Z (CZ), or iSWAP, create quantum correlations between different qubits. This is a key advantage over classical sequential models, as entanglement allows the circuit to establish direct, non-local relationships between features, regardless of their position in a sequence. This provides a powerful mechanism for learning complex, system-wide dependencies that can be difficult for classical recurrent architectures to capture effectively. Second, parametrised single-qubit rotations are the primary mechanism for embedding the learnable parameters of the model. They locally transform the state of each qubit, providing nuanced control to adapt the quantum state during optimisation. The ability to use a small number of these rotational parameters to manipulate a state in a high-dimensional space represents a potential advantage in model compactness and trainability compared to classical neural networks, which may require a significantly larger number of parameters for similar expres-

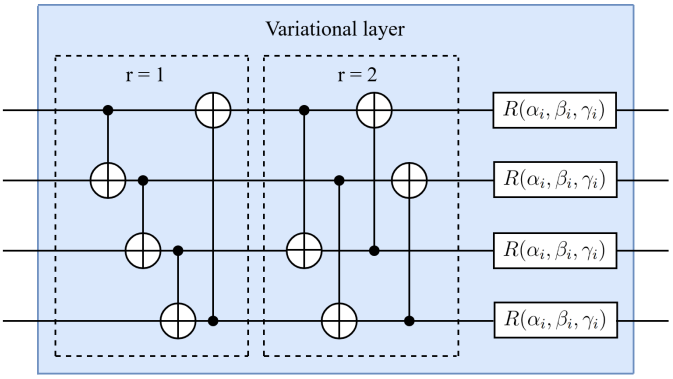

Fig. 5: The structure of the variational layer.

sive power. The structure of the variational layer used in this paper is shown in Fig. 5. The CNOT gate is a two-qubit gate that flips the second qubit (the target qubit) when the first qubit (the control qubit) is $|1\rangle$, while leaving the second qubit unchanged when the first qubit state is $|0\rangle$. The CNOT gate has a matrix representation as

$$\text{CNOT} = \begin{bmatrix} 1 & 0 & 0 & 0 \\ 0 & 1 & 0 & 0 \\ 0 & 0 & 0 & 1 \\ 0 & 0 & 1 & 0 \end{bmatrix}. \tag{14}$$

The action of the CNOT gate can be described as

$$\text{CNOT}: \begin{cases} |00\rangle \mapsto |00\rangle, \\ |01\rangle \mapsto |01\rangle, \\ |10\rangle \mapsto |11\rangle, \\ |11\rangle \mapsto |10\rangle. \end{cases} \tag{15}$$

First, CNOT gates are applied among the qubits to create entanglement. The control qubit is n and the target qubit is $(n+r)$ mod N, where r is a hyperparameter that defines the entanglement range. In this work, $r = 1$ and $r = 2$ are used to define our entanglement strategy. This specific architecture creates two layers of entanglement, which balances expressivity with a reasonable circuit depth. For $r = 1$, the state $|\chi_2\rangle$ is transformed into $|\chi_3\rangle$ as follows:

$$|\chi_3\rangle = \prod_{n=1}^{N} \text{CNOT}_{n,(n+1) \bmod N} |\chi_2\rangle. \tag{16}$$

For $r = 2$, the state $|\chi_3\rangle$ is transformed into $|\chi_4\rangle$ as follows:

$$|\chi_4\rangle = \prod_{n=1}^{N} \text{CNOT}_{n,(n+2) \bmod N} |\chi_3\rangle. \tag{17}$$

Second, for each qubit, a parametrised rotation gate $R(\alpha_n, \beta_n, \gamma_n)$ is applied, where $R(\alpha_n, \beta_n, \gamma_n) = R_x(\alpha_n) R_y(\beta_n) R_z(\gamma_n)$ and α_n, β_n, and γ_n are trainable parameters. Rotation gate $R_x(\vartheta)$ rotates a qubit around the x-axis of the Bloch sphere. Its matrix representation is given by

$$R_x(\vartheta) = \begin{bmatrix} \cos(\vartheta/2) & -i\sin(\vartheta/2) \\ -i\sin(\vartheta/2) & \cos(\vartheta/2) \end{bmatrix}. \tag{18}$$

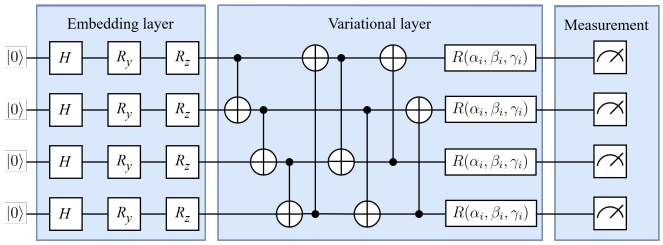

Fig. 6: The structure of the VQC.

After applying the parametrised rotations, the state $|\chi_4\rangle$ is transformed into $|\chi_5\rangle$ as follows:

$$|\chi_5\rangle = \prod_{n=1}^{N} R(\alpha_n, \beta_n, \gamma_n) |\chi_4\rangle. \tag{19}$$

After the variational layer, the quantum state $|\chi_5\rangle$ is processed through the measurement layer. The measurement layer serves as the interface for extracting classical information from the final quantum state. To achieve this, this work utilises the expectation value of the Pauli-Z operator. This method provides a continuous output value in the range of $[-1, 1]$, which represents the statistical tendency of the qubit to be in the $|0\rangle$ state versus the $|1\rangle$ state. This offers a nuanced characterisation of the final quantum state. The continuous nature of this output makes it compatible with the gradient-based optimisation methods used for training hybrid quantum-classical models. The Pauli-Z operator is represented as

$$Z = \begin{bmatrix} 1 & 0 \\ 0 & -1 \end{bmatrix}, \tag{20}$$

where the eigenvalues $+1$ and -1 correspond to the qubit being in state $|0\rangle$ and $|1\rangle$, respectively. The expected value of the Pauli-Z operator for the quantum state $|\xi\rangle$ is given by

$$\langle Z \rangle = \langle \xi | Z | \xi \rangle. \tag{21}$$

This expected value determines whether the qubit is more likely to be in state $|0\rangle$ or $|1\rangle$. The calculated expected values, which lie in the range $[-1, 1]$, are classical numerical outputs that can be directly processed by the classical layers in the hybrid model. This approach allows us to extract numerical values directly from the quantum system for further analysis. Using the Pauli-Z-based measurement provides a reliable method for extracting quantum data for further computation. Overall, the VQC offers three key advantages for the channel estimation problem addressed in this work: first, quantum superposition enables the simultaneous processing of diverse signal features; second, quantum entanglement allows the circuit to model complex interdependencies among these features; and third, the parametrised nature of VQCs provides adaptability similar to classical neural networks while potentially offering computational advantages through quantum parallelism. Fig. 6 illustrates the complete structure of the VQCs embedded within the QLSTM cell, comprising a data embedding layer, a variational layer, and a measurement layer.

C. An Integrated CNN-QLSTM Model

While LSTMs (QLSTMs) are particularly effective at capturing long-term dependencies within sequential data, their design does not inherently accommodate the extraction or processing of spatial features. To address the channel estimation problem in the RIS-NOMA system discussed in Section IV, a combination of QLSTMs with CNNs is proposed. CNNs have gained prominence in ML due to their strong capability to process and understand visual data [73]. The architecture of CNNs is characterised by several layers that work synergistically: convolutional layers apply filters to detect and extract features from the input data, pooling layers reduce both the dimensionality of the data and computational complexity while preserving important information, and fully connected layers integrate these extracted features to make predictions. This multi-layered structure enables CNNs to effectively learn hierarchical data representations and identify complex patterns, making them well-suited for tasks such as image classification, object detection, and segmentation. In addition to their effectiveness in processing visual data, CNNs are also employed for time-series analysis and forecasting because they can identify local patterns and structures in temporal data [74]. Nonetheless, they tend to be less effective at capturing long-range temporal relationships, a challenge for which LSTMs (QLSTMs) are better suited. The integration of CNNs with QLSTMs offers a systematic approach for addressing the dual challenges of spatial and temporal modelling in RIS-NOMA channel estimation. In this context, spatial features represent the structured relationships among signal components across different dimensions, specifically, the magnitude and phase values distributed among multiple users. CNNs are used to learn these spatial patterns from each input instance by identifying local correlations and hierarchical feature representations. Conversely, temporal dependencies reflect the dynamic evolution of these spatial features across successive time steps. QLSTMs are specifically designed to model these temporal sequences. Here, the quantum-enhanced nature of the QLSTM provides a distinct advantage: the underlying VQCs can capture highly complex and non-linear temporal dependencies with potentially greater efficiency and fewer parameters than a classical LSTM. This allows for a more compact yet powerful model for learning the intricate evolution of the wireless channel. The proposed CNN-QLSTM integrated model, illustrated in Fig. 7, consists of two modules: a CNN module and a QLSTM module. This architectural design reflects the natural decomposition of the channel estimation problem into spatial feature extraction followed by temporal sequence modelling. The CNN module comprises two two-dimensional (2D) convolutional (Conv2D) layers, a max-pooling (MP) layer and a flatten (FL) layer. Each convolutional layer applies multiple learnable filters (or kernels) to scan the input data, performing dot products between the filters and local regions of the input. This process generates feature maps, which highlight the presence and location of various features within the input. Following the convolutional layers, an MP layer is utilised to downsample the feature maps, reducing their size to improve computational efficiency while preserving key features. MP partitions the feature maps into non-overlapping regions and retains the maximum value from each region. The output from the MP layer is flattened into a one-dimensional vector by the FL layer and subsequently reshaped into a temporal sequence with t_2 output time steps, effectively transforming the spatial feature representations into a format suitable for sequential processing by the QLSTM module. The QLSTM module processes this temporally-structured input through two layers. The first QLSTM layer captures temporal dependencies and patterns within the input sequence. The second QLSTM layer further refines these representations to capture more complex temporal dependencies and patterns. Finally, a linear output layer maps the refined hidden state representations to the target output dimension.

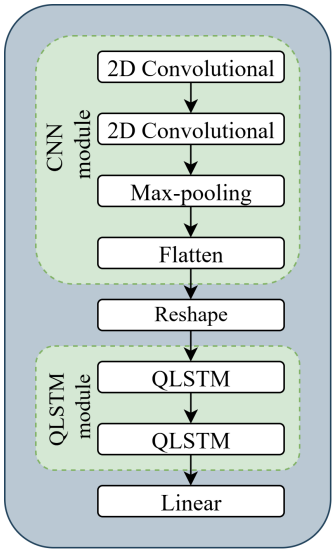

Fig. 7: The structure of the proposed CNN-QLSTM model.

D. Model Training

The RIS-NOMA system is modelled with a single-antenna BS ($S = 1$), a RIS, and $K = 2$ users with a single antenna each ($Q = 1$). We set the reference distance d_0 to 20 m, the BS-RIS distance d_s to 150 m, while the RIS–user distances d_{r1} and d_{r2} are set respectively to 30 m and 40 m. In this work, $x(t)$ and $\mathbf{H}_1(t)$ follow the distribution $\mathcal{CN} \sim (1, 0.1)$. $\mathbf{H}_{21}(t)$ and $\mathbf{H}_{22}(t)$ follow $\mathcal{CN} \sim (4, 1)$ and $\mathcal{CN} \sim (3, 1)$, respectively. The amplitude reflection coefficient κ_r is set to 1, indicating that no energy loss within the context of lossless metasurfaces. Since our time-series datasets are particularly sensitive to fluctuations, the phase shifts φ_r are generated within a range of $[0.01\pi, 0.02\pi]$. The performance of the proposed CNN-QLSTM model is evaluated in different RIS-NOMA scenarios including varying power allocation factors $\zeta = [0.1 : 0.05 : 0.35]$, SNR $\rho = [10 : 2.5 : 20]$, the number of RIS elements $R = [20 : 10 : 70]$. All system-level parameters are outlined in Tab. II. In the CNN module, the first Conv2D layer uses two filters of size 3×3 with "same" padding. The second Conv2D layer applies one 3×3 filter, also with "same" padding. An MP layer with a 2×2 pooling kernel is then

TABLE II: Simulation parameters.

Parameters	Symbols	Values
Number of antennas at BS	S	1
Number of users	K	2
Number of antennas at each U_k	Q	1
Constant speed per time step	v	0.1 m
Amplitude reflection coefficient	κ_r	1
Phase shift	φ_r	$[0.01\pi, 0.02\pi]$
PLE from BS to RIS	τ_s	2.2
PLE from RIS to U_k	τ_{rk}	2.2
Dataset length	D'	2000
Number of input time steps into CNN module	t_1	20
Number of output time steps from CNN module	t_2	1
Power allocation factor	ζ	$[0.1 : 0.05 : 0.35]$
SNR	ρ	$[10 : 2.5 : 20]$ dB
Number of RIS elements	R	$[20 : 10 : 70]$

employed. In the QLSTM module, both QLSTM layers have 16 units. The Linear layer produces an output dimension of 2, which corresponds to the cascaded channel gains of two users. For each RIS-NOMA scenario, the dataset is first normalised in the range between 0 and 1 and then split into 80% training and 20% testing data. The proposed CNN-QLSTM model is trained up to 100 epochs to minimise the MSE, which is calculated as follows:

$$\text{MSE} = \frac{1}{n}\sum_{i=1}^{n}(y_i - \widehat{y}_i)^2, \tag{22}$$

where n is the number of data points, while y_i and $\widehat{y}_i$ are the actual and predicted values for the i-th data point, respectively. The parameters are updated via an adaptive gradient (Adagrad) optimisation algorithm. The parameter update rule [75] is mathematically expressed as

$$\theta_{e+1,i} = \theta_{e,i} - \frac{\lambda}{\sqrt{G_{e,ii}} + \epsilon} \cdot \nabla_{\theta_{e,i}} J(\theta_{e,i}), \tag{23}$$

where $\theta_{e,i}$ is the current parameter, λ is the initial learning rate, $G_{e,ii}$ is the accumulated sum of squared gradients for the i-th parameter, and ϵ is a small constant added to avoid division by zero (e.g., 10^{-8}). In this paper, λ is set to 0.05.

E. Evaluation Metrics

After training the model, the performance of the proposed CNN-QLSTM model is evaluated on the test dataset using three different metrics: root mean square error (RMSE), mean absolute error (MAE), and mean absolute percentage error (MAPE). The selection of these three complementary metrics provides a comprehensive evaluation framework for RIS-NOMA channel estimation: RMSE penalises larger errors more heavily, which is critical since significant channel estimation errors can severely impact SIC performance in NOMA systems; MAE provides robust average accuracy assessment; and MAPE enables scale-independent comparison across different system configurations and operating conditions. The RMSE metric is defined as

$$\text{RMSE} = \sqrt{\frac{1}{n}\sum_{i=1}^{n}(\widehat{y}_i - y_i)^2}. \tag{24}$$

The MAE metric is calculated as

$$\text{MAE} = \frac{1}{n}\sum_{i=1}^{n}\left|\widehat{y}_i - y_i\right|. \tag{25}$$

Both RMSE and MAE are scale-dependent metrics, which have limitations in comparing models across datasets with different scales, while MAPE measures the error as a percentage of the actual values, making it a scale-free metric. The MAPE metric is expressed as:

$$\text{MAPE} = \frac{1}{n}\sum_{i=1}^{n}\left|\frac{y_i - \widehat{y}_i}{y_i}\right| \times 100. \tag{26}$$

In Eq. (24) and Eq. (25), $\widehat{y}_i$ represents the predicted value, y_i represents the actual value, and n is the number of data points. MAPE offers a more generalized and interpretable measure of the performance of the proposed model. Lower values of RMSE, MAE, and MAPE indicate better model performance, with MAPE values below 10% considered to reflect a good level of prediction. Dataset generation, model training, and evaluation processes are implemented using PyTorch, while PennyLane is used for constructing and integrating the quantum circuits. To synthesise the entire methodology, the complete end-to-end workflow is illustrated in Fig. 8. This schematic provides a visual summary of the key stages of our framework, including the data generation and preprocessing steps detailed in Section IV, as well as the architecture of the proposed CNN-QLSTM model, and the training and evaluation procedures described in this section.

F. Selection of the VQC Architecture

The performance of the proposed model is influenced by various factors, including the architecture of the VQC. In this work, we investigate different circuit architectures, including variations in the number of qubits and embedding strategies, to identify an optimal configuration for our model.

1) Model Performance Under Different Numbers of Qubits: To determine the optimal number of qubits for the CNN-QLSTM model, five CNN-QLSTM models are constructed, each using VQCs with a different number of qubits, ranging from 2 to 6. Type 3 (4 qubits) is represented in Fig. 6. Other types are depicted in Fig. 9. The RIS-NOMA system configuration is set to $\rho = 15$ dB, $R = 20$, $\zeta = 0.3$. The performance of these five models is evaluated on the test dataset using RMSE, MAE, and MAPE as shown in Tab. III.

TABLE III: Performance of CNN-QLSTM models with different numbers of qubits.

Types of VQC	No. of qubits	RMSE	MAE	MAPE
Type 1	2	0.01264	0.01112	0.09831
Type 2	3	0.01129	0.00961	0.08509
Type 3	**4**	**0.00676**	**0.00553**	**0.04798**
Type 4	5	0.01068	0.00907	0.07967
Type 5	6	0.01076	0.00925	0.08164

The table presents the average values of RMSE, MAE, and MAPE metrics for user 1 and user 2. The model with 4 qubits demonstrated the best balance between model complexity and the ability to capture relevant patterns in the

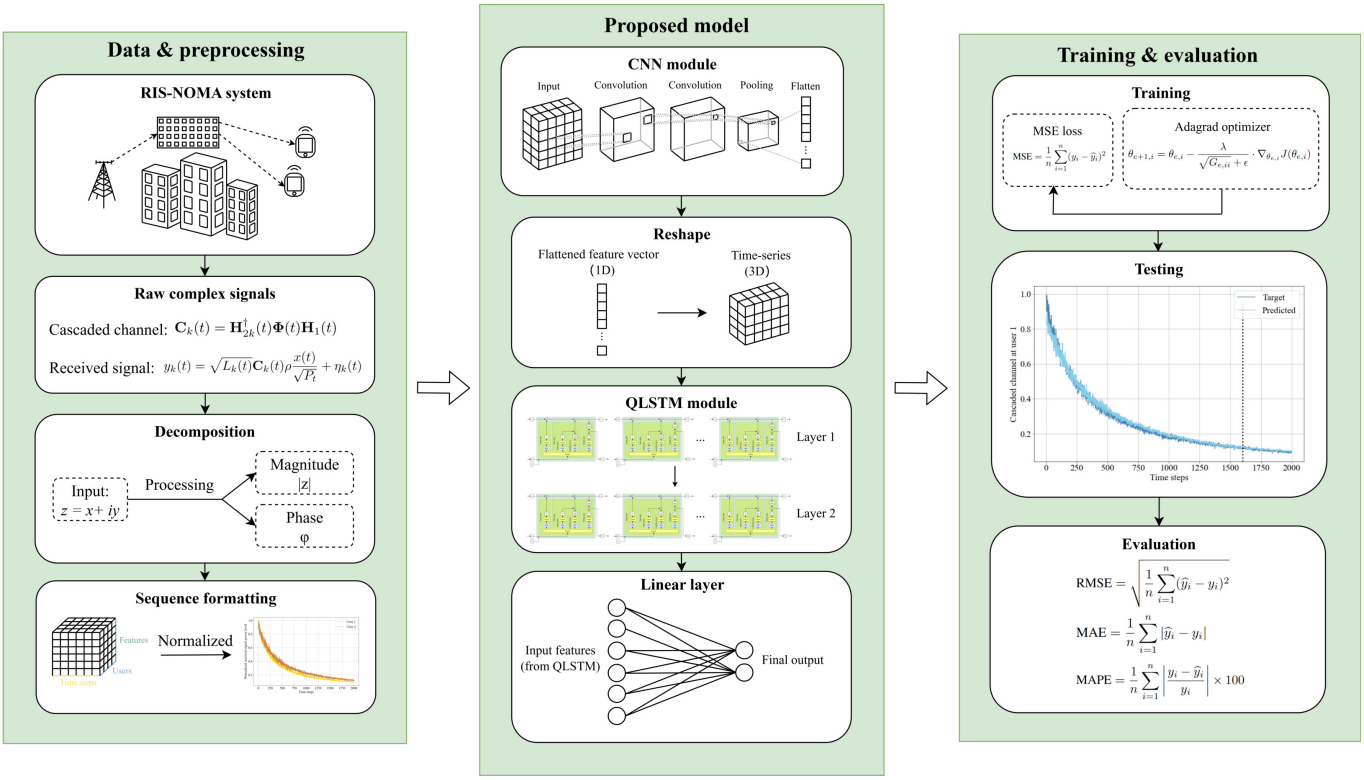

Fig. 8: Overall workflow of the proposed channel estimation framework.

dataset. This balance allowed it to generalise well without apparent instability or significant degradation in predictive performance. In comparison, models with 2 or 3 qubits showed limited capacity to capture the complexity of the data, which resulted in poorer performance. Meanwhile, models with 5 or 6 qubits, although more complex, faced challenges such as instability during training and diminished generalisation ability. Increasing the number of qubits can also lead to more complex optimisation landscapes, which can negatively affect training and generalisation. Based on these observations, the model with 4 qubits achieved the best performance among the five models evaluated.

2) Model Performance Under Different Types of Quantum Embedding: To select an appropriate quantum embedding technique, four CNN-QLSTM models are constructed, each using VQCs with a different type of quantum embedding, as shown in Fig. 10. Embedding type 1 consists of Hadamard gates followed by rotation gates R_y, where the classical input vector is encoded as the rotation angles of the R_y gates. Similarly, embedding type 2 consists of Hadamard gates followed by rotation gates R_z, encoding the classical input vector as the rotation angles of the R_z gates. Embedding type 3 has been introduced previously in Section V-B. In embedding type 4, Hadamard gates are applied to each qubit, followed by rotation gates R_z, where the n-th feature u_n of the input vector $\overrightarrow{u} = (u_1, u_2, \ldots, u_N)$ is encoded as the rotation angle. Subsequently, RZZ gates are implemented on qubits n and m, where $n \in [1, \ldots, N-1]$ and $m \in [n+1, \ldots, N]$. Each RZZ gate consists of two CNOT gates and an R_z gate with a rotation angle $u_n u_m$. The RIS-NOMA system configuration is also set to $\rho = 15$ dB, $R = 20$, $\zeta = 0.3$. The performance of these four models is evaluated on the test dataset using RMSE, MAE and MAPE as shown in Tab. IV.

TABLE IV: Performance of CNN-QLSTM models with different quantum embedding techniques.

Types of embedding	RMSE	MAE	MAPE
Type 1	0.01293	0.01085	0.09619
Type 2	0.01251	0.01080	0.09483
Type 3	**0.00676**	**0.00553**	**0.04798**
Type 4	0.01021	0.00868	0.07686

Each value in the table represents the average of the RMSE, MAE, and MAPE metrics calculated for both user 1 and user 2. The results from Tab. IV show that embedding type 3 has the best overall performance with the lowest RMSE, MAE and MAPE values. Type 1 and type 2, which apply only one type of rotation gates (either R_y or R_z), show higher errors, indicating that they offer less flexibility in representing the complex input features. While type 4 shows reasonable performance, it is less effective than type 3 as shown by its higher higher RMSE, MAE, and MAPE values. With its use of additional entanglement and controlled operations, it may introduce challenges in training or optimisation. As a result, embedding type 3, with moderate complexity, provides the best balance between feature representation and model performance. Therefore, for the remainder of this paper, the 4-qubit quantum circuit employing embedding type 3 will be used, as it provides an effective balance between complexity and performance across the evaluated metrics.

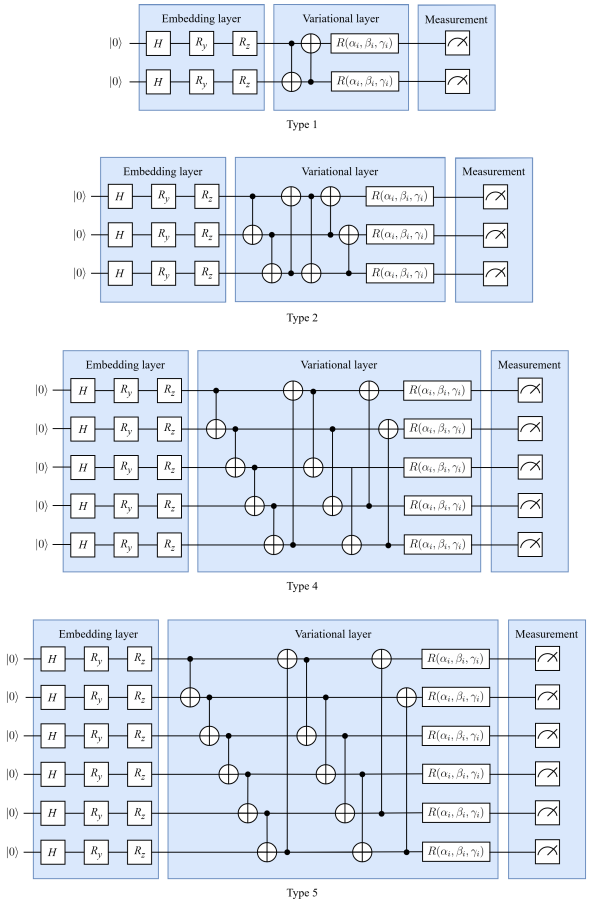

Fig. 9: Types of VQCs.

VI. Results and Discussion

In this section, simulation results of the proposed CNN-QLSTM model across various RIS-NOMA system configurations are provided.

A. Model Performance Under a Specific RIS-NOMA Scenario

The performance of the CNN-QLSTM model is evaluated under a system configuration with the SNR of 15 dB, 20 RIS elements, and the power allocation factor of 0.3. The magnitude of the normalised received signals at two users over 2000 time steps is shown in Fig. 11. Additionally, Fig. 12 illustrates the MSE loss up to 100 epochs on the normalised training dataset. The training loss in Fig. 12 indicates that the CNN-QLSTM model learns effectively throughout the training process. There is a sharp decline in the loss over the first few epochs, showing that the model quickly identifies important patterns in the data. Although the training loss continues to decrease, it reaches approximately 0.0002 at the 90th epoch and begins to stabilise, with minimal variation up to the 100th epoch. Fig. 13 presents the prediction performance of the CNN-QLSTM model for user 1 on both the training and testing datasets. Here, the dotted line visually represents the division between the training and testing datasets. As shown in Tab. III and Tab. IV, the CNN-QLSTM model shows strong performance with an average RMSE of 0.00676, MAE of 0.00553 and MAPE of 0.04798. These values indicate that the model predicts with high accuracy across different metrics.

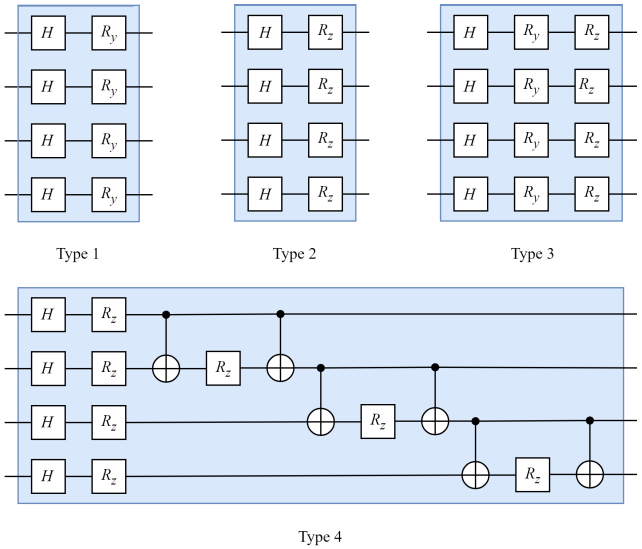

Fig. 10: Types of quantum embedding techniques.

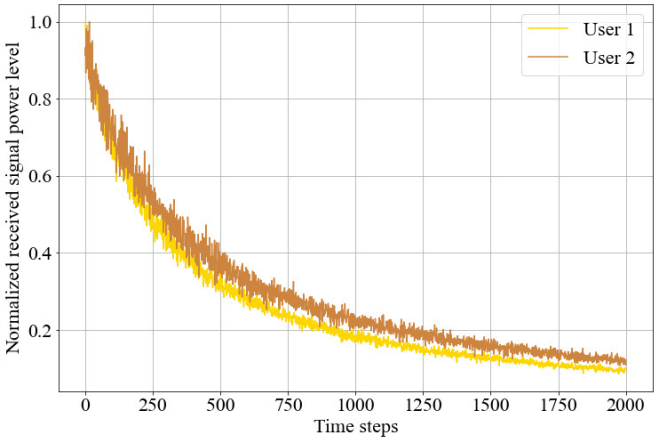

Fig. 11: The normalised magnitude of the received signals at two users under the SNR of 15 dB with 20 RIS elements, and the power allocation factor of 0.3.

B. Model Performance Under Varying Power Allocation Factors

In this subsection, the performance of the CNN-QLSTM model is analysed under different power allocation factors while maintaining the SNR of 15 dB and 20 RIS elements. Fig. 14, Fig. 15, and Fig. 16 illustrate the respective RMSE, MAE, and MAPE values on the test dataset. Each figure presents the values of the respective metric for both individual users and their average. These figures show a consistent decrease in RMSE, MAE, and MAPE for both users as the power allocation factor increases. User 2 exhibits higher RMSE and MAE values compared to user 1, while user 1 shows higher MAPE values. RMSE and MAE measure the absolute difference between the predicted and actual values. Higher values for user 2 suggest that the magnitude of the

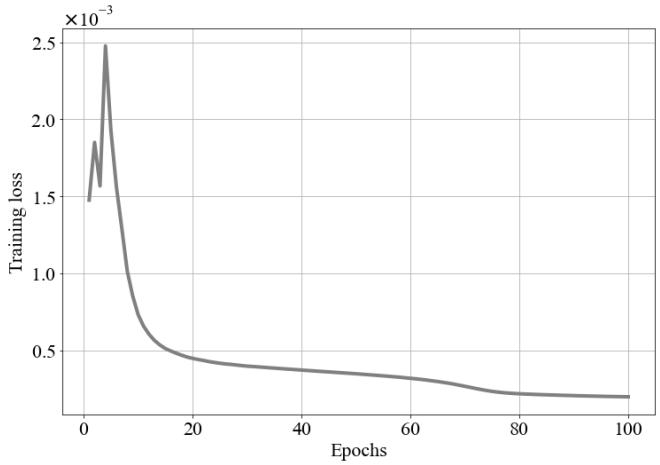

Fig. 12: Training loss under the SNR of 15 dB with 20 RIS elements, and the power allocation factor of 0.3.

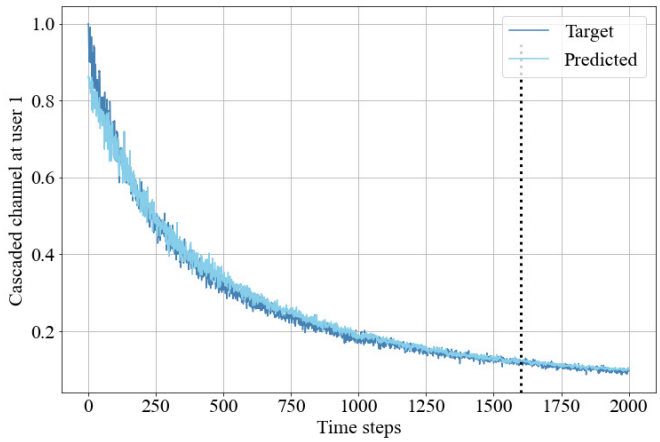

Fig. 13: Prediction performance for user 1 under the SNR of 15 dB with 20 RIS elements, and the power allocation factor of 0.3.

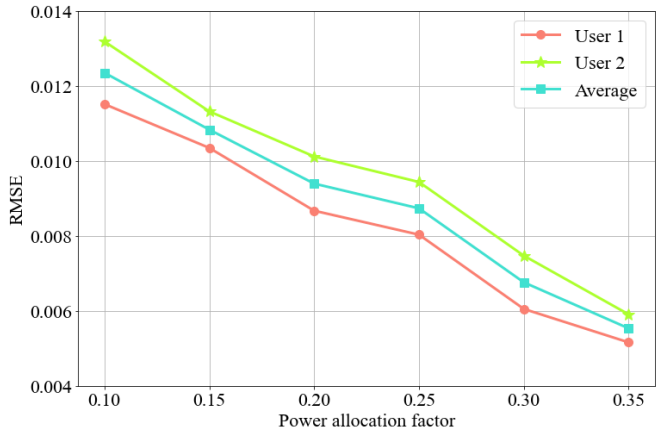

Fig. 14: RMSE values under varying power allocation factors at the SNR of 15 dB with 20 RIS elements.

prediction errors is greater for user 2 than for user 1. In contrast, MAPE normalises the error by the actual value, making it more sensitive to the relative size of the error in

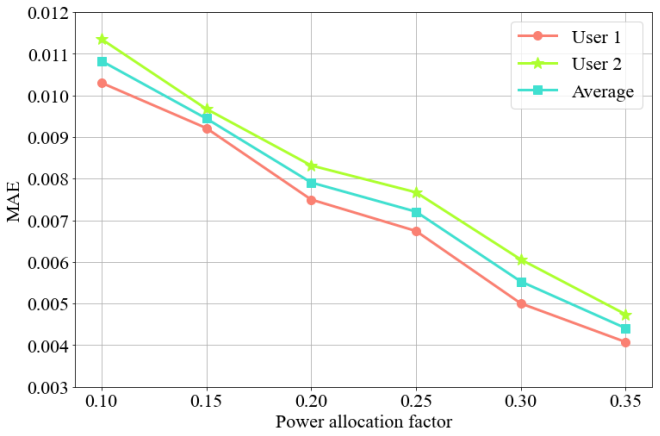

Fig. 15: MAE values under varying power allocation factors at the SNR of 15 dB with 20 RIS elements.

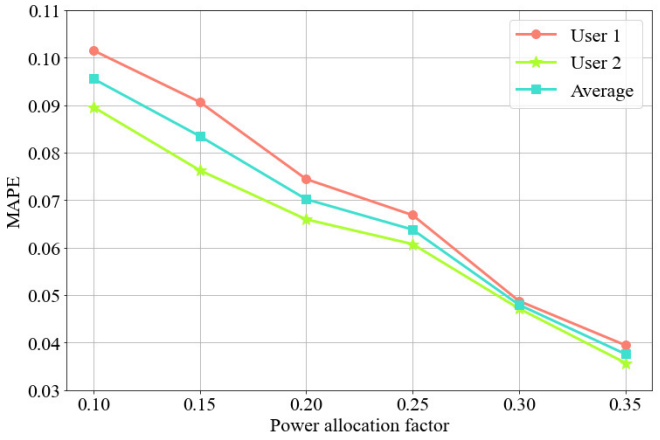

Fig. 16: MAPE values under varying power allocation factors at the SNR of 15 dB with 20 RIS elements.

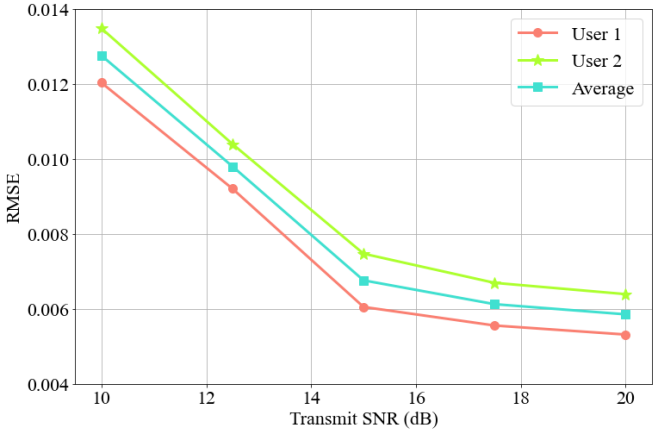

Fig. 17: RMSE values under varying SNR with 20 RIS elements and the power allocation factor of 0.3.

proportion to the true value. The higher MAPE for user 1 indicates that even though the absolute errors are smaller, they represent a larger percentage of the actual values.

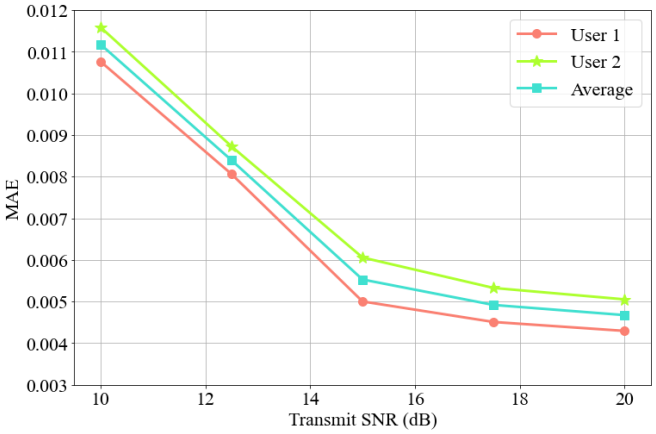

Fig. 18: MAE values under varying SNR with 20 RIS elements and the power allocation factor of 0.3.

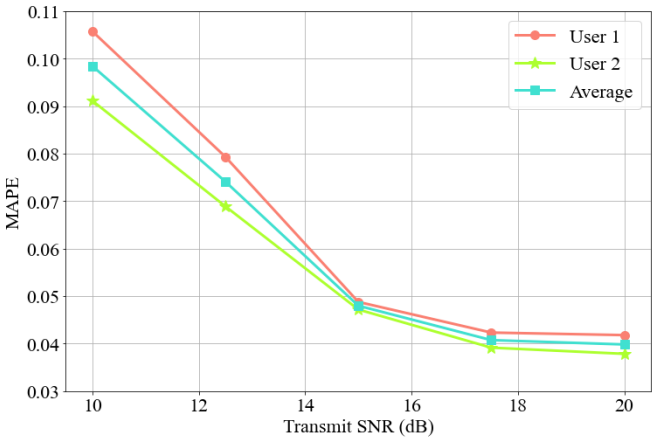

Fig. 19: MAPE values under varying SNR with 20 RIS elements and the power allocation factor of 0.3.

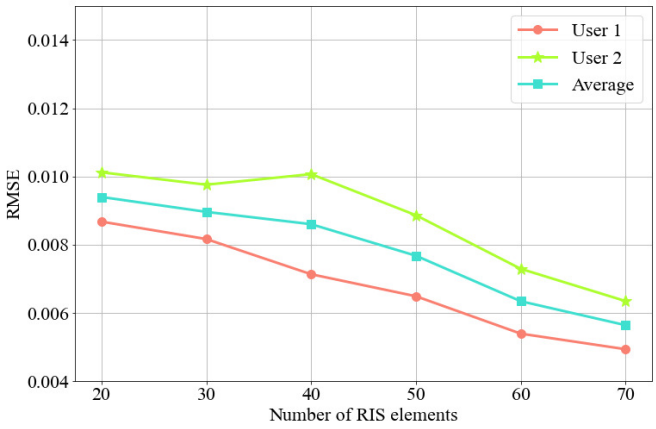

Fig. 20: RMSE values under varying numbers of RIS elements at the SNR of 15 dB and the power allocation factor of 0.2.

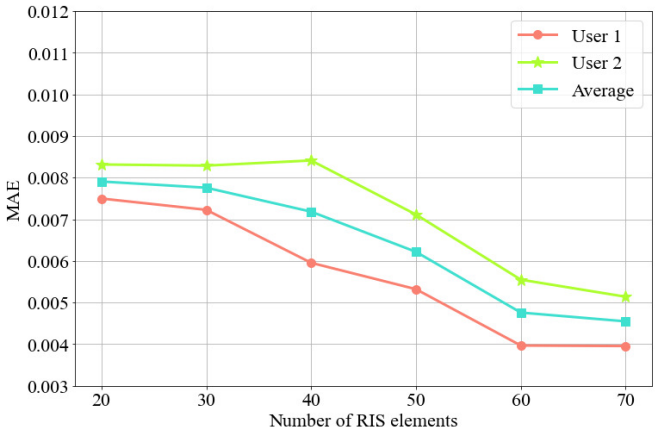

Fig. 21: MAE values under varying numbers of RIS elements at the SNR of 15 dB and the power allocation factor of 0.2.

C. Model Performance Under Varying SNRs

This subsection analyses the performance of the CNN-QLSTM model for SNR values ranging from 10 to 20 dB, with 20 RIS elements and the power allocation factor of 0.3. Fig. 17, Fig. 18, and Fig. 19 show the respective RMSE, MAE, and MAPE values on the test dataset. Each figure presents the individual values for each user as well as their average. The figures show that as the SNR increases, RMSE, MAE, and MAPE consistently decrease for both users. A higher SNR indicates a stronger signal relative to the noise, which leads to a more reliable communication environment for users. Similar to the case of increasing the power allocation factor, user 2 has higher RMSE and MAE values compared to user 1, while user 1 shows higher MAPE values.

D. Model Performance Under Varying Number of RIS Elements

In this subsection, the performance of the CNN-QLSTM model is analysed by varying the number of RIS elements from 20 to 70, while keeping the SNR at 15 dB and the power allocation factor at 0.2. Fig. 20, Fig. 21, and Fig. 22 represent the RMSE, MAE, and MAPE values, respectively, on the test dataset. Each figure presents the results for each user and their average. The results across all three metrics indicate that increasing the number of RIS elements improves the performance of the model for both users, though the impact varies between them. In Fig. 20 and Fig. 21, RMSE and MAE generally decrease as the number of RIS elements increases. However, when the number of RIS elements is 40, a slight increase in both RMSE and MAE is observed for user 2. The slight increase is attributed to a higher variability within the dataset generated for the $R = 40$ configuration.

E. Comparison of the Proposed Model With Other Models

This section compares the channel estimation performance of the proposed CNN-QLSTM model with other quantum and classical models that have been applied for this task. To provide a pure quantum benchmark, we implement a standalone QNN. For a fair comparison, this QNN uses the same optimal 4-qubit VQC architecture (type 3) established in Fig. 9 in Section V-F. However, the model incorporates 2 variational layers with CNOT entanglement and rotation gates. This provides a direct comparison with pure quantum-inspired methods to evaluate the benefit of our hybrid classical-quantum approach. Additionally, we evaluate our approach

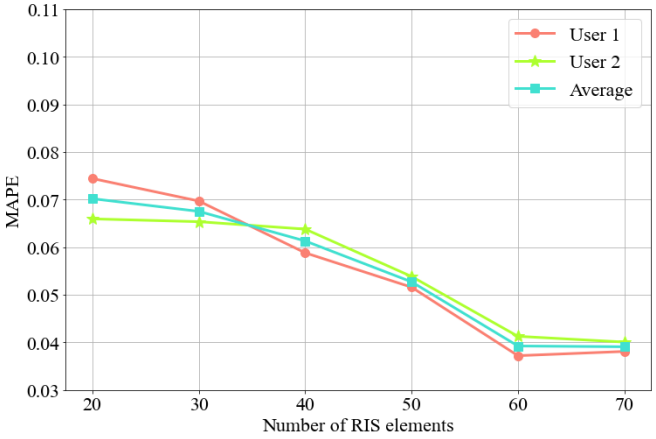

Fig. 22: MAPE values under varying numbers of RIS elements at the SNR of 15 dB and the power allocation factor of 0.2.

against four classical DL models commonly used in wireless communication scenarios: CNN [33], LSTM [76], BiLSTM [77], and CNN-LSTM [34]. To ensure a fair comparison, CNN-LSTM follows the same structure as our proposed model, while all other models are implemented with two layers. The CNN model follows the same structure as the CNN module in our proposed approach, while each layer in the LSTM and BiLSTM models consists of 16 units. The evaluation is conducted under the same RIS-NOMA system configuration as in Section VI-A, with the SNR of 15 dB, 20 RIS elements, and the power allocation factor of 0.3. Performance is also assessed using three standard metrics: RMSE, MAE, and MAPE. The averaged values for RMSE, MAE, and MAPE for both users across all evaluated models are presented in Tab. V.

TABLE V: Performance comparison of different models.

Models	RMSE	MAE	MAPE
QNN	0.01056	0.00912	0.07756
CNN	0.00971	0.00783	0.06922
LSTM	0.00889	0.00733	0.06477
BiLSTM	0.00815	0.00671	0.05900
CNN-LSTM	0.00773	0.00618	0.05345
CNN-QLSTM	**0.00676**	**0.00553**	**0.04798**

The results in Tab. V present the performance comparison of the proposed model with the quantum-inspired baseline and classical DL models for channel estimation in the defined RIS-NOMA system configuration. The results indicate that the proposed CNN-QLSTM model consistently outperforms all baseline models across all evaluation metrics. The pure QNN baseline achieves the worst performance among all evaluated models. This indicates that pure quantum approaches struggle significantly with the complex characteristics of RIS-NOMA data. The poor performance of the standalone QNN suggests that quantum circuits alone require additional architectural components to effectively handle the high-dimensional nature of wireless channel estimation tasks. Among the classical models, the CNN-LSTM model achieves the best performance, with an RMSE of 0.00773 and a MAPE of 0.05345. However, its performance remains worse than that of the CNN-QLSTM model since the integration of VQCs within the QLSTM module enables more efficient temporal modelling and improves overall accuracy. The BiLSTM model achieves a slightly worse performance than that of the CNN-LSTM model, with an RMSE of 0.00815 and a MAPE of 0.05900, demonstrating the advantages of combining CNNs for spatial feature extraction with LSTMs for efficient temporal modelling. The bidirectional structure of the BiLSTM model, which processes temporal dependencies from both past and future time steps, improves estimation accuracy compared to the standard LSTM model. Although the LSTM model is effective in capturing sequential dependencies, it performs slightly worse than the BiLSTM model, with an RMSE of 0.00889. The absence of bidirectional processing limits its ability to fully exploit temporal information. The CNN model achieves the highest RMSE of 0.00971 and MAPE of 0.06922, which shows that spatial feature extraction alone is insufficient for accurate channel estimation. Since the CNN model does not inherently model sequential dependencies, it struggles to capture the dynamic nature of wireless channel variations over time. The comparison demonstrates that the hybrid approach effectively combines the advantages of both classical and quantum processing, whilst pure quantum or classical methods alone show limitations in this complex estimation task. Overall, the consistent superior performance of the proposed CNN-QLSTM model across all evaluation metrics highlights its effectiveness in overcoming the inherent challenges of channel estimation in RIS-NOMA systems.

To evaluate the computational complexity of the proposed CNN-QLSTM model relative to the other baseline models, we compare the number of trainable parameters and model size, as shown in Tab. VI.

TABLE VI: Complexity comparison of different models.

Models	Trainable parameters	Model Size
QNN	54	0.21 KB
CNN	306	1.19 KB
LSTM	3618	14.11 KB
BiLSTM	9282	36.26 KB
CNN-LSTM	6146	24.01 KB
CNN-QLSTM	**778**	**3.04 KB**

The number of trainable parameters for each model is obtained using the `model.parameters()` function in PyTorch, and the corresponding model size is computed based on the memory required to store these parameters. Among the models, the BiLSTM model has the highest complexity due to its bidirectional structure, whereas the LSTM model, though simpler, still requires a substantial number of parameters to model temporal dependencies. The QNN baseline demonstrates the lowest computational complexity with only 54 trainable parameters and 0.21 KB model size, reflecting the compact nature of pure quantum circuits. However, this minimal complexity comes at the cost of significantly reduced performance. The CNN model, primarily designed for spatial feature extraction, is relatively simple due to the absence of re-

current connections. The CNN-LSTM model, which combines both convolutional and recurrent layers, is computationally less demanding than BiLSTM but remains more complex than standalone CNN, QNN and LSTM models. Despite incorporating quantum-enhanced processing, the proposed CNN-QLSTM maintains a compact architecture with a relatively low number of parameters, effectively balancing computational cost and estimation accuracy. These results demonstrate the efficiency of CNN-QLSTM, making it well-suited for practical deployment in RIS-NOMA systems, where lightweight models are essential for real-time channel estimation.

Although the proposed CNN-QLSTM model demonstrates superior performance compared to classical approaches under the evaluated system configuration and shows consistent performance across varying system configurations, several challenges must be investigated before practical deployment in real-world 6G environments. This context highlights a critical trade-off for practical deployment: the superior estimation accuracy offered by the quantum-enhanced architecture must be weighed against the near-term challenges of hardware noise, classical-quantum interface latency, and the computational overhead of running quantum circuits. While our model shows promise in simulated environments, its real-world feasibility will depend on the continued maturation of quantum hardware and the development of more efficient optimisation techniques that mitigate these practical constraints. First, hardware constraints and quantum noise effects present significant obstacles, as current quantum computing hardware suffers from limited qubit coherence times, gate fidelities, and susceptibility to environmental decoherence, which can degrade the performance advantages observed in idealised simulations. Addressing these hardware limitations is an active area of research. Potential mitigation strategies range from near-term software-based approaches, such as quantum error mitigation techniques that estimate and compensate for the effects of noise from the final results, to the long-term development of quantum error correction codes, which aim to create fault-tolerant quantum computers. Furthermore, designing variational algorithms and quantum circuits to be inherently more resilient to the specific noise characteristics of a given hardware platform is another promising direction. Moreover, limited access to quantum hardware represents a practical barrier, as quantum computers remain expensive and are not widely accessible to researchers and practitioners, potentially hindering widespread adoption and validation of quantum-enhanced approaches. Second, scalability concerns arise when extending the approach to large-scale RIS-assisted networks with hundreds of elements and numerous users, as the quantum circuit complexity and classical-quantum interface overhead may offset computational benefits. Third, computational overhead optimisation remains challenging, particularly in balancing the quantum circuit depth with estimation accuracy while maintaining real-time processing requirements typical in wireless communications. Fourth, the integration of quantum and classical processing components introduces synchronisation and latency challenges that must be addressed for practical channel estimation applications. Fifth, extending the framework to accommodate multi-user and multi-RIS scenarios introduces additional complexity in quantum state preparation and measurement procedures. In addition to these technical challenges, several broader challenges exist within the research ecosystem. Sixth, the lack of standardisation in quantum model implementation poses significant difficulties, as there are no established guidelines or unified frameworks for designing quantum-enhanced machine learning architectures, leading to inconsistent approaches and difficulties in reproducing and comparing results across different studies. Seventh, the absence of standardised procedures for defining and implementing 6G system parameters creates additional uncertainty, as both quantum computing and 6G technologies are rapidly evolving fields with continuously changing specifications and requirements. Finally, developing more sophisticated quantum embedding strategies that can efficiently represent the high-dimensional and dynamic nature of wireless channel data remains an open research direction. These challenges reflect the nascent state of both quantum machine learning and 6G technologies, where standardisation efforts and best practices are still evolving. Researchers investigating QML applications in 6G channel estimation should systematically address these challenges to bridge the gap between theoretical quantum advantages and practical wireless system deployment.

VII. Conclusion

This paper presents the CNN-QLSTM, a hybrid quantum-classical ML model for channel estimation in RIS-NOMA systems. The integration of CNNs for spatial feature extraction and QLSTM networks for temporal modelling enables the proposed model to effectively capture both spatial correlations and sequential patterns within the received signal features. The variational quantum circuit (VQC) used in the QLSTM is formulated with a detailed mathematical description, including the quantum embedding process, entanglement mechanism, parametrised quantum operations, and measurement process. To identify the optimal VQC architecture that ensures the efficiency of the proposed model, multiple VQC configurations were explored through extensive simulations that evaluated the performance of the model under various system configurations. The study examines the impact of key system parameters, including SNR, power allocation factors, and the number of RIS elements, on estimation accuracy. The findings suggest that higher SNR, optimised power allocation, and an increased number of RIS elements generally lead to improved estimation accuracy achieved by the CNN-QLSTM framework. These results demonstrate the robustness of the proposed model across different RIS-NOMA system configurations. Furthermore, simulation results confirm that CNN-QLSTM achieves better estimation accuracy compared to both pure quantum and classical DL-based estimators, including the QNN, CNN, LSTM, and BiLSTM, in terms of RMSE, MAE, and MAPE.

This study offers valuable insights into the application of QML-based techniques for channel estimation in RIS-NOMA systems, demonstrating their effectiveness in achieving more precise estimation performance. However, practical implementation in real-world wireless networks remains an open challenge. Future research should focus on refining quantum

embedding strategies to enhance the representation of classical data in the quantum domain, optimising the VQC structure to reduce computational overhead, and improving model scalability for large-scale RIS-assisted networks. Additionally, extending the proposed framework to accommodate multi-user and multi-RIS scenarios will be essential for broader applicability. Further investigations into hardware constraints, quantum noise effects, and hybrid classical-quantum optimisation techniques could also contribute to the feasibility of QML in next-generation 6G networks. The findings in this work establish a foundation for integrating QML into wireless communication systems, supporting its practical deployment in future communication technologies.

ACKNOWLEDGEMENTS

This work was supported in part by the Canada Excellence Research Chair (CERC) Program CERC-2022-00109, in part by the Natural Sciences and Engineering Research Council of Canada (NSERC) Discovery Grant Program RGPIN-2025-04941, and in part by the NSERC Collaborative Research and Training Experience (CREATE) Program (Grant number 596205-2025). The work of O. A. Dobre was supported in part by the Canada Research Chair Program CRC-2022-00187. The work of B. Canberk was partially supported by The Scientific and Technological Research Council of Turkey (TUBITAK) 1515 Frontier R&D Laboratories Support Program for BTS Advanced AI Hub: BTS Autonomous Networks and Data Innovation Lab. Project 5239903.

REFERENCES

[1] C.-X. Wang *et al.*, "On the road to 6G: Visions, requirements, key technologies, and testbeds," *IEEE Commun. Surveys Tuts.*, vol. 25, no. 2, pp. 905–974, Apr. 2023.

[2] I. F. Akyildiz, C. Han, Z. Hu, S. Nie, and J. M. Jornet, "Terahertz band communication: An old problem revisited and research directions for the next decade," *IEEE Trans. Commun.*, vol. 70, no. 6, pp. 4250–4285, Jun. 2022.

[3] Z. Wan, Z. Gao, F. Gao, M. D. Renzo, and M.-S. Alouini, "Terahertz massive MIMO with holographic reconfigurable intelligent surfaces," *IEEE Trans. Commun.*, vol. 69, no. 7, pp. 4732–4750, Jul. 2021.

[4] K. B. Letaief, Y. Shi, J. Lu, and J. Lu, "Edge artificial intelligence for 6G: Vision, enabling technologies, and applications," *IEEE J. Sel. Areas Commun.*, vol. 40, no. 1, pp. 5–36, Jan. 2022.

[5] O. B. Akan, E. Dinc, M. Kuscu, O. Cetinkaya, and B. A. Bilgin, "Internet of everything (IoE) - from molecules to the universe," *IEEE Commun. Mag.*, vol. 61, no. 10, pp. 122–128, Oct. 2023.

[6] Y. Cheng, K. H. Li, Y. Liu, K. C. Teh, and H. V. Poor, "Downlink and uplink intelligent reflecting surface aided networks: NOMA and OMA," *IEEE Trans. Wirel. Commun.*, vol. 20, no. 6, pp. 3988–4000, Jun. 2021.

[7] Y. Liu *et al.*, "Evolution of NOMA toward next generation multiple access (NGMA) for 6G," *IEEE J. Sel. Areas Commun.*, vol. 40, no. 4, pp. 1037–1071, Apr. 2022.

[8] B. Zheng, Q. Wu, and R. Zhang, "Intelligent reflecting surface-assisted multiple access with user pairing: NOMA or OMA?" *IEEE Commun. Lett.*, vol. 24, no. 4, pp. 753–757, Apr. 2020.

[9] A. Almohamad *et al.*, "Smart and secure wireless communications via reflecting intelligent surfaces: A short survey," *IEEE Open J. Commun. Soc.*, vol. 1, pp. 1442–1456, Sep. 2020.

[10] J. Zuo, Y. Liu, Z. Qin, and N. Al-Dhahir, "Resource allocation in intelligent reflecting surface assisted NOMA systems," *IEEE Trans. Commun.*, vol. 68, no. 11, pp. 7170–7183, Nov. 2020.

[11] Y. Liu *et al.*, "Reconfigurable intelligent surfaces: Principles and opportunities," *IEEE Commun. Surveys Tuts.*, vol. 23, no. 3, pp. 1546–1577, 3rd Quart. 2021.

[12] S. Basharat *et al.*, "Reconfigurable intelligent surfaces: Potentials, applications, and challenges for 6G wireless networks," *IEEE Wireless Commun.*, vol. 28, no. 6, pp. 184–191, Dec. 2021.

[13] Y. Zhang *et al.*, "Generative adversarial networks based digital twin channel modeling for intelligent communication networks," *China Commun.*, vol. 20, no. 8, pp. 32–43, Aug. 2023.

[14] C. Luo, J. Ji, Q. Wang, X. Chen, and P. Li, "Channel state information prediction for 5G wireless communications: A deep learning approach," *IEEE Trans. Netw. Sci. Eng.*, vol. 7, no. 1, pp. 227–236, Jan.–Mar. 2020.

[15] K. Weththasinghe, B. Jayawickrama, and Y. He, "Machine learning-based channel estimation for 5G new radio," *IEEE Wireless Commun. Lett.*, vol. 13, no. 4, pp. 1133–1137, Apr. 2024.

[16] G. Yang, X. Xu, Y.-C. Liang, and M. D. Renzo, "Reconfigurable intelligent surface-assisted non-orthogonal multiple access," *IEEE Trans. Wireless Commun.*, vol. 20, no. 5, pp. 3137–3151, May 2021.

[17] W. Shen, Z. Qin, and A. Nallanathan, "Deep learning for super-resolution channel estimation in reconfigurable intelligent surface aided systems," *IEEE Trans. Commun.*, vol. 71, no. 3, pp. 1491–1503, Mar. 2023.

[18] M. K. Shehzad, L. Rose, S. Wesemann, and M. Assaad, "ML-based massive MIMO channel prediction: Does it work on real-world data?" *IEEE Wireless Commun. Lett.*, vol. 11, no. 4, pp. 811–815, Apr. 2022.

[19] J. Fan, P. Liang, Z. Jiao, and X. Han, "A compressive sensing and deep learning-based time-varying channel estimation for FDD massive MIMO systems," *IEEE Trans. Veh. Technol.*, vol. 71, no. 8, pp. 8729–8738, Aug. 2022.

[20] C. Zuo, H. Deng, J. Zhang, and Y. Qi, "Distributed channel estimation algorithm for mmwave massive MIMO communication systems," in *Proc. 2021 IEEE 94th Veh. Technol. Conf. (VTC2021-Fall)*, Sep. 2021, pp. 1–6.

[21] T. Q. Duong *et al.*, "Quantum-inspired machine learning for 6G: Fundamentals, security, resource allocations, challenges, and future research directions," *IEEE Open J. Veh. Technol.*, vol. 3, pp. 375–387, Aug. 2022.

[22] T. M. Khan and A. Robles-Kelly, "Machine learning: Quantum vs classical," *IEEE Access*, vol. 8, pp. 219 275–219 294, Dec. 2020.

[23] S. J. Nawaz, S. K. Sharma, S. Wyne, M. N. Patwary, and M. Asaduzzaman, "Quantum machine learning for 6G communication networks: State-of-the-art and vision for the future," *IEEE Access*, vol. 7, pp. 46 317–46 350, Apr. 2019.

[24] J. B. Thomas, S. G. Chaudhari, S. K. V., and N. K. Verma, "CNN-based transformer model for fault detection in power system networks," *IEEE Trans. Instrum. Meas.*, vol. 72, pp. 1–10, Jan. 2023.

[25] Z. Ali *et al.*, "Enhancing performance of movie recommendations using LSTM with meta path analysis," *IEEE Access*, vol. 11, pp. 119 017–119 032, Oct. 2023.

[26] O. Rubasinghe *et al.*, "A novel sequence to sequence data modelling based CNN-LSTM algorithm for three years ahead monthly peak load forecasting," *IEEE Trans. Power Syst.*, vol. 39, no. 1, pp. 1932–1947, Jan. 2024.

[27] S. Y.-C. Chen, S. Yoo, and Y.-L. L. Fang, "Quantum long short-term memory," in *Proc. of the IEEE Int. Conf. Acoust., Speech, Signal Process.*, May 2022, pp. 8622–8626.

[28] C. Xu *et al.*, "Channel estimation for reconfigurable intelligent surface assisted high-mobility wireless systems," *IEEE Trans. Veh. Technol.*, vol. 72, no. 1, pp. 718–734, Jan. 2023.

[29] T. T. Vu, T. Van Chien, C. T. Dinh, H. Quoc Ngo, and M. Matthaiou, "Channel estimation in RIS-assisted downlink massive MIMO: A learning-based approach," in *Proc. 2022 IEEE 23rd Int. Workshop Signal Process. Advances Wireless Communi. (SPAWC)*, Oulu, Finland, Jul. 2022, pp. 1–5.

[30] Z. Gu, C. He, Z. Huang, and M. Xiao, "Channel estimation for IRS aided MIMO system with neural network solution," in *Proc. 2023 IEEE 98th Veh. Technol. Conf. (VTC2023-Fall)*, Hong Kong, Hong Kong, Oct. 2023.

[31] A. Nayak, M. Sarkar, S. Sahoo, and S. Nanda, "Channel estimation of MIMO-NOMA system based on a variable forgetting factor recursive least square algorithm," in *Proc. 2021 IEEE 2nd Int. Conf. Appl. Electromagn., Signal Process., Commun. (AESPC)*, Bhubaneswar, India, Nov. 2021.

[32] M. Alayu, M. Sarkar, and S. Nanda, "5G channel estimation of NOMA-OFDM system using arctangent LMS algorithm," in *Proc. 2023 2nd Int. Conf. Comput. Syst. Commun. (ICCSC)*, Thiruvananthapuram, India, Mar. 2023.

[33] T. S. Anu and T. Raveendran, "CNN-based channel estimation using NOMA for mmwave massive MIMO system," in *Proc. IEEE Stat. Signal Process. Workshop (SSP)*, Hanoi, Vietnam, Jul. 2023.

[34] C. Nguyen, T. M. Hoang, and A. A. Cheema, "Channel estimation using CNN-LSTM in RIS-NOMA assisted 6G network," *IEEE Trans. Mach. Learn. Commun. Netw.*, vol. 1, pp. 43–60, May 2023.

[35] H. Sadia, H. Iqbal, S. Fawad Hussain, and N. Saeed, "Signal detection in intelligent reflecting surface-assisted NOMA network using LSTM model: A ML approach," *IEEE Open J. Commun. Soc.*, vol. 6, pp. 29–38, Dec. 2024.

[36] E. Vlachos and K. Blekos, "Quantum computing-assisted channel estimation for massive MIMO mmwave systems," in *Proc. 2022 IFIP/IEEE 30th Int. Conf. Very Large Scale Integr. (VLSI-SoC)*, Patras, Greece, Oct. 2022.

[37] B. Narottama and S. Aïssa, "Modular quantum machine learning for channel estimation in STAR-RIS assisted communication systems," in *Proc. 2023 IEEE 34th Annu. Int. Symp. Pers. Indoor Mobile Radio Commun. (PIMRC)*, Sep. 2023, pp. 1–6.

[38] W. Gao, W. Zhang, L. Liu, and M. Yang, "Deep residual learning with attention mechanism for OFDM channel estimation," *IEEE Wireless Communications Letters*, vol. 14, no. 2, pp. 250–254, Feb. 2025.

[39] H.-P. Yin, X.-H. Zhao, J.-L. Yao, and H.-P. Ren, "Deep-learning-based channel estimation for chaotic wireless communication," *IEEE Wireless Commun. Lett,*, vol. 13, no. 1, pp. 143–147, Jan. 2024.

[40] A. S. M. M. Jameel, A. Malhotra, A. E. Gamal, and S. Hamidi-Rad, "Deep OFDM channel estimation: Capturing frequency recurrence," *IEEE Commun. Lett.*, vol. 28, no. 3, pp. 562–566, Mar. 2024.

[41] J. Li *et al.*, "Deep learning-assisted OFDM channel estimation and signal detection technology," *IEEE Commun. Lett.*, vol. 27, no. 5, pp. 1347–1351, May 2023.

[42] Q. Zhao, X. Zeng, Z. Fan, Q. Zhang, and W. Li, "Channel estimation for FDD massive MIMO with complex residual denoising network," *IEEE Wireless Commun. Lett,*, vol. 13, no. 8, pp. 2070–2074, Aug. 2024.

[43] W. Huang *et al.*, "A spatial-specific neural network-based OFDM channel estimation under time-varying channels," *IEEE Wireless Commun. Lett.*, vol. 12, no. 12, pp. 2183–2187, Dec. 2023.

[44] M. Gaballa, M. Abbod, and S. Alnasur, "Hybrid deep learning for channel estimation and power allocation for MISO-NOMA system," in *Proc. 2022 IEEE Future Netw. World Forum (FNWF)*, Montreal, QC, Canada, Oct. 2022.

[45] L. Dai and X. Wei, "Distributed machine learning based downlink channel estimation for RIS assisted wireless communications," *IEEE Trans. Commun.*, vol. 70, no. 7, pp. 4900–4909, Jul. 2022.

[46] H. Feng and Y. Zhao, "mmwave RIS-assisted SIMO channel estimation based on global attention residual network," *IEEE Wireless Communications Letters*, vol. 12, no. 7, pp. 1179–1183, Jul. 2023.

[47] H. Feng, Y. Xu, and Y. Zhao, "Deep learning-based joint channel estimation and CSI feedback for RIS-assisted communications," *IEEE Commun. Lett.*, vol. 28, no. 8, pp. 1860–1864, Aug. 2024.

[48] A. T. Dogukan, E. Arslan, and E. Basar, "Reconfigurable intelligent surface-enabled downlink NOMA," *IEEE Trans. Wireless Commun.*, vol. 23, no. 11, pp. 16 950–16 961, Nov. 2024.

[49] M. H. Kumar, S. Sharma, K. Deka, and M. Thottappan, "Reconfigurable intelligent surfaces assisted hybrid NOMA system," *IEEE Commun. Lett.*, vol. 27, no. 1, pp. 357–361, Jan. 2023.

[50] K.-T. Nguyen, T.-H. Vu, and S. Kim, "A unified framework analysis for reconfigurable intelligent surface-aided coordinated NOMA systems," *IEEE Trans. Veh. Technol.*, vol. 72, no. 11, pp. 15 115–15 120, 2023.

[51] W. Wei, X. Pang, C. Xing, N. Zhao, and D. Niyato, "STAR-RIS aided secure NOMA integrated sensing and communication," *IEEE Trans. Wireless Commun.*, vol. 23, no. 9, pp. 10 712–10 725, Sep. 2024.

[52] L. Liu, H. Wang, and R. Song, "Optimization for multi-cell NOMA systems assisted by multi-RIS with inter-RIS reflection," *IEEE Commun. Lett.*, vol. 28, no. 1, pp. 123–127, Jan. 2024.

[53] H. Al-Obiedollah, H. B. Salameh, K. Cumanan, Z. Ding, and O. A. Dobre, "Competitive IRS assignment for IRS-based NOMA system," *IEEE Wireless Commun. Lett.*, vol. 13, no. 2, pp. 505–509, Feb. 2024.

[54] D. K. P. Asiedu and J.-H. Yun, "Multiuser NOMA with multiple reconfigurable intelligent surfaces for backscatter communication in a symbiotic cognitive radio network," *IEEE Trans. Veh. Technol.*, vol. 72, no. 4, pp. 5300–5316, Apr. 2023.

[55] Y. Cheng *et al.*, "Performance analysis and power allocation for covert mobile edge computing with RIS-aided NOMA," *IEEE Trans. Mobile Comput.*, vol. 23, no. 5, pp. 4212–4227, May 2024.

[56] H. Zhao *et al.*, "Air reconfigurable intelligent surface enhanced multiuser NOMA system," *IEEE Internet Things J.*, vol. 11, no. 1, pp. 29–39, Jan. 2024.

[57] A. P. Chrysologou, A.-A. A. Boulogeorgos, and N. D. Chatzidiamantis, "When THz-NOMA meets holographic reconfigurable intelligent surfaces," *IEEE Commun. Lett.*, vol. 27, no. 9, pp. 2516–2520, Sep. 2023.

[58] Z. Han, X. Yue, B. Dai, R. Liu, and A. Nallanathan, "Reconfigurable intelligent surface assisted unified NOMA framework," *IEEE Trans. Veh. Technol.*, vol. 72, no. 8, pp. 10 617–10 632, Aug. 2023.

[59] X. Li *et al.*, "Performance analysis of double reconfigurable intelligent surfaces assisted NOMA networks," *IEEE Trans. Veh. Technol.*, vol. 73, no. 12, pp. 18 732–18 747, Nov. 2024.

[60] Y. Pei *et al.*, "Secrecy performance analysis of multi-functional RIS-assisted NOMA networks," *IEEE Trans. Wireless Commun.*, vol. 24, no. 2, pp. 1648–1662, Feb. 2025.

[61] M. O. Butt, N. Waheed, T. Q. Duong, and W. Ejaz, "Quantum-inspired resource optimization for 6G networks: A survey," *IEEE Commun. Surveys Tuts.*, pp. 1–1, Dec. 2024.

[62] T. Q. Duong *et al.*, "Quantum-inspired real-time optimization for 6G networks: Opportunities, challenges, and the road ahead," *IEEE Open J. Commun. Soc.*, vol. 3, pp. 1347–1359, Aug. 2022.

[63] M. Xu *et al.*, "Quantum-secured space-air-ground integrated networks: Concept, framework, and case study," *IEEE Wireless Commun.*, vol. 30, no. 6, pp. 136–143, Dec. 2023.

[64] ——, "Privacy-preserving intelligent resource allocation for federated edge learning in quantum internet," *IEEE J. Sel. Topics Signal Process.*, vol. 17, no. 1, pp. 142–157, Jan. 2023.

[65] F. Zaman, U. Khalid, T. Q. Duong, H. Shin, and M. Z. Win, "Quantum full-duplex communication," *IEEE J. Sel. Areas Commun.*, vol. 41, no. 9, pp. 2966–2980, Sep. 2023.

[66] B. Hazarika, K. Singh, O. A. Dobre, C.-P. Li, and T. Q. Duong, "Quantum-enhanced federated learning for metaverse-empowered vehicular networks," *IEEE Trans. Commun.*, pp. 1–1, Nov. 2024.

[67] S. Tariq *et al.*, "Deep quantum-transformer networks for multimodal beam prediction in ISAC systems," *IEEE Internet Things J.*, vol. 11, no. 18, pp. 29 387–29 401, Sep. 2024.

[68] A. Paul *et al.*, "Quantum-enhanced DRL optimization for DoA estimation and task offloading in ISAC systems," *IEEE J. Sel. Areas Commun.*, vol. 43, no. 1, pp. 364–381, Jan. 2025.

[69] A. Paul, K. Singh, C.-P. Li, O. A. Dobre, and T. Q. Duong, "Digital twin-aided vehicular edge network: A large-scale model optimization by quantum-DRL," *IEEE Trans. Veh. Technol.*, vol. 74, no. 2, pp. 2156–2173, Feb. 2025.

[70] Y. Han, N. Li, Y. Liu, T. Zhang, and X. Tao, "Artificial noise aided secure NOMA communications in STAR-RIS networks," *IEEE Wireless Commun. Lett.*, vol. 11, no. 6, pp. 1191–1195, Jun. 2022.

[71] Y. Pei *et al.*, "Secrecy outage probability analysis for downlink RIS-NOMA networks with on-off control," *IEEE Trans. Veh. Technol.*, vol. 72, no. 9, pp. 11 772–11 786, Sep. 2023.

[72] W. Kong *et al.*, "Short-term residential load forecasting based on LSTM recurrent neural network," *IEEE Trans. Smart Grid*, vol. 10, no. 1, pp. 841–851, Jan. 2019.

[73] Z.-Q. Zhao, P. Zheng, S.-T. Xu, and X. Wu, "Object detection with deep learning: A review," *IEEE Trans. Neural Netw. Learn. Syst*, vol. 30, no. 11, pp. 3212–3232, Nov. 2019.

[74] C. Nguyen *et al.*, "Deep learning models for time-series forecasting of RF-EMF in wireless networks," *IEEE Open Journal of the Communications Society*, vol. 5, pp. 1399–1414, 2024.

[75] J. C. Duchi, E. Hazan, and Y. Singer, "Adaptive subgradient methods for online learning and stochastic optimization," *J. Mach. Learn. Res.*, vol. 12, pp. 2121–2159, Jul. 2011.

[76] M. A. Razaz, A. Q. Algaolahi, M. A. Makarem, and E. H. Alwardy, "VLC channel estimation for indoor environment using LSTM," in *Proc. 2024 4th Inte. Conf. Emerg. Smart Technol. Appl. (eSmarTA)*, Sana'a, Yemen, Aug. 2024.

[77] A. K. Nair and V. Menon, "Joint channel estimation and symbol detection in MIMO-OFDM systems: A deep learning approach using Bi-LSTM," in *Proc. 2022 14th Int.l Conf. on Commun. Syst. NETw. (COMSNETS)*, Bangalore, India, Jan. 2022, pp. 406–411.